

Developmental decrease of entorhinal gate disrupts prefrontal-hippocampal communication in immune-challenged DISC1 knockdown mice

Xi Xia Xu

University Medical Center Hamburg-Eppendorf

Lingzhen Song

University Medical Center Hamburg-Eppendorf

Rebecca Kringel

University Medical Center Hamburg-Eppendorf

Ileana Hanganu-Opatz (✉ hangop@zmnh.uni-hamburg.de)

University Medical Center Hamburg-Eppendorf

Article

Keywords: prefrontal-hippocampal dysfunction, prefrontal-hippocampal communication

Posted Date: March 10th, 2021

DOI: <https://doi.org/10.21203/rs.3.rs-290304/v1>

License:  This work is licensed under a Creative Commons Attribution 4.0 International License.

[Read Full License](#)

Version of Record: A version of this preprint was published at Nature Communications on November 23rd, 2021. See the published version at <https://doi.org/10.1038/s41467-021-27114-w>.

1
2 **Developmental decrease of entorhinal gate disrupts**
3 **prefrontal-hippocampal communication in immune-**
4 **challenged DISC1 knockdown mice**

5
6
7 Xiaxia Xu*, Lingzhen Song, Rebecca Kringel, and Ileana L. Hanganu-Opatz*

8
9 *Institute of Developmental Neurophysiology, Center for Molecular Neurobiology, University*
10 *Medical Center Hamburg-Eppendorf, 20251 Hamburg, Germany*
11

12
13 **Running title:** Abnormal entorhinal gate of developing circuits

14
15 *Corresponding authors: Ileana L. Hanganu-Opatz
16 hangop@zmnh.uni-hamburg.de

17
18 Xiaxia Xu
19 xiaxia.xu@zmnh.uni-hamburg.de
20

21
22
23
24 Figures: 7

25 Tables: 1

26 Number of pages: 40

27 Number of words in Abstract: 150

28 Number of words in Introduction: 789

29 Number of words in Discussion: 954
30

31 Abstract

32 The prefrontal-hippocampal dysfunction that underlies cognitive deficits in mental disorders
33 emerges during early development. The contribution of the lateral entorhinal cortex (LEC), a
34 gatekeeper of prefrontal cortex (PFC) and hippocampus (HP), to the early dysfunction is fully
35 unknown. Here we show that the poorer LEC-dependent associative recognition memory
36 detectable at pre-juvenile age is preceded by abnormal communication within LEC-HP-PFC
37 networks of neonatal mice mimicking the combined genetic and environmental etiology (GE)
38 of disease. The prominent entorhinal drive to HP is weaker in GE mice as a result of sparser
39 projections from LEC to CA1 and decreased efficiency of axonal terminals to activate the
40 hippocampal circuits. In contrast, the direct entorhinal drive to PFC is not affected in GE
41 mice, yet the PFC is indirectly compromised, as target of the under-activated HP. Thus,
42 already at neonatal age, the entorhinal function gating prefrontal-hippocampal circuits is
43 impaired in a mouse model of disease.

44 INTRODUCTION

45 The major burden of major psychiatric disorders, such as schizophrenia, is a lifelong
46 cognitive disability^{1, 2}. Its devastating impact on the daily life is augmented by the fact that
47 the available medication causes a weak, if any, improvement of cognitive deficits concerning
48 attention, speed of processing, working and long-term memory, executive function, and
49 social cognition, despite (almost) complete resolution of psychotic symptoms³. The
50 pathophysiological substrate of these deficits has been identified to center on the prefrontal-
51 hippocampal network^{4, 5}. Abnormal prefrontal-hippocampal coupling during the tasks has
52 been described in schizophrenia patients^{4, 6}. It relates not only to local alterations at
53 microscopic and macroscopic scales in both areas⁷ but also to connectivity dysfunction
54 within large-scale networks⁸. In particular, the interactions between HP and entorhinal cortex,
55 which tightly communicate with each other along reciprocal pathways⁹, have been tackled in
56 clinical and neuropathological investigations^{10, 11, 12, 13}. While some findings are still
57 controversial, cytoarchitectural disorganization, cellular and synaptic deficits in layer 2 as
58 well as aberrant axonal innervation have been detected in the entorhinal cortex of
59 schizophrenia patients^{14, 15}. It has been hypothesized that they result from developmental
60 disturbance of migration, differentiation and wiring of entorhinal circuits. However, the
61 underlying mechanisms of these deficits and their contribution to the cognitive impairment
62 are currently unknown.

63 Broader network dysconnectivity as underlying mechanism of cognitive deficits has
64 been also identified in rodent models of mental illness^{16, 17, 18}. While these models vary in
65 their etiology, utility and validity, they provide precious insights into the neural basis of
66 cognitive deficits that are difficult to obtain in humans¹⁹, especially when considering areas
67 poorly investigated and less accessible, such as the entorhinal cortex. Lesion of the lateral
68 entorhinal cortex (LEC) caused disease-characteristic altered mesolimbic dopaminergic
69 transmission^{20, 21}. Being a direct correlate of cognitive performance²², gamma oscillations
70 within entorhinal-hippocampal circuits have been found to be disrupted in mouse models of
71 disease²³.

72 Besides providing insights into the neurobiological substrate of disease, mouse
73 models enable to test the neurodevelopmental origin of schizophrenia-related deficits.
74 Recently, we showed that already during early postnatal development the neuronal activity
75 and communication between limbic brain areas is profoundly compromised in a mouse
76 model mimicking the genetic (knock-down of Disrupted-In-Schizophrenia 1 (*Disc1*)²⁴) and
77 environmental (maternal immune activation (MIA)) etiology (GE) of mental illness^{25, 26, 27, 28}.
78 Weaker communication between PFC and HP at neonatal age results from dysfunction of
79 local pyramidal-interneuronal interactions as well as sparsification of hippocampal
80 projections targeting the PFC^{28, 29, 30}. At this age, LEC boosts the prefrontal-hippocampal
81 circuits by projecting to PFC and HP³¹ and facilitating their oscillatory entrainment³².
82 However, an in-depth characterization of the early network function and communication of
83 LEC with PFC-HP pathway in disease models of mental illness is currently lacking.

84 To address this knowledge gap, here we combine *in vivo* electrophysiology and
85 optogenetics with anatomical tracing and behavioral investigation to interrogate the
86 developing entorhinal-hippocampal-prefrontal circuits in a mouse model mimicking the
87 genetic and environmental etiology of mental illness. We show that in neonatal GE mice,
88 sparser and less efficient projections from LEC cause weaker activation of HP and indirectly,
89 of its target, the PFC.

90 **RESULTS**

91 **Pre-juvenile GE mice have poorer associative recognition memory**

92 One of the traits of cognitive impairment in schizophrenia is the poorer associative memory
93 identified both in first episode and chronic patients³³. This memory form requires precisely
94 timed interactions within entorhinal-hippocampal circuits in humans³⁴ and mice³⁵. The strong
95 lateral entorhinal input to HP provides non-spatial (contextual) information and facilitates the
96 binding of information relating to objects, places, and contexts. To get first insights into the
97 LEC function towards the end of development, we assessed the associative memory in GE
98 when compared to control (CON) mice of pre-juvenile age (postnatal day (P) 17-18). For this,

99 two tasks were used: (i) novel object preference (distinct objects) (NOPd) task that involves
100 an association between two different objects and (ii) object-location preference (OLP) task
101 that involves an association between object and location (Fig. 1a, b). Mice performing these
102 tasks showed an augmented neural activity in LEC mirrored by stronger cFos expression
103 (supplementary fig. 1), suggesting that these two associative recognition tasks relates to
104 LEC activation.

105 To test whether GE mice show poorer LEC-dependent associative recognition
106 memory, we investigated CON (n = 20) and GE (n = 16) mice in NOPd and OLP tasks using
107 a custom-designed arena. In line with our previous data³⁶, we initiated the investigation after
108 full maturation of sensory and motor abilities required for processing of novelty (P17). During
109 the familiarization trial of the NOPd task, all mice spent equal time investigating the two
110 objects placed in the arena (Fig. 1a). During the test trial, both CON mice and GE mice
111 spent significantly longer time interacting with the novel object (CON: 146.66 ± 9.42 s, $p =$
112 0.0009 , discrimination = 0.52 ± 0.06 ; GE: 115.89 ± 7.06 s, $p = 0.04$, discrimination = $0.26 \pm$
113 0.09) than with the familiar one (CON: 60.80 ± 7.22 s; GE: 93.03 ± 12.93 s) (Fig. 1a).
114 However, GE mice had a poorer object discrimination when compared to CON mice (one-
115 way ANOVA, $F_{(1,38)} = 6.95$, $p = 0.012$). The behavioral impairment was detected only when
116 the genetic deficit was paired with MIA and absent in one-hit G (*Disc1* mutation alone) and
117 one-hit E (MIA alone) mice that performed equally well as CON mice (supplementary fig. 2a).
118 During the OLP task, the pre-juvenile mice had to associate object and location and
119 distinguish, which object was placed in a newer location (Fig. 1b). In the test trial, the CON
120 mice spent significantly longer time with the object with a newer location (new: 129.73 ± 6.07
121 s, old: 70.03 ± 7.75 s, $p = 0.007$, discrimination = 0.34 ± 0.07). GE mice equally investigated
122 both objects (new: 102.94 ± 6.06 s, old: 74.42 ± 12.16 s, $p = 0.09$, discrimination = $0.10 \pm$
123 0.09). Correspondingly, the object discrimination was significantly lower in GE mice than in
124 CON mice (one-way ANOVA, $F_{(1,38)} = 4.86$, $p = 0.034$). One-hit G and one-hit E mice were
125 also unable to recognize the object with a newer location (supplementary fig. 2b).

126 Poor performance in NOPd and OLP tasks may result not only specifically from
127 dysfunction of entorhinal networks but also from poorer motor abilities and/or enhanced
128 anxiety when interacting with the objects. To exclude these confounding effects, we
129 analyzed the exploratory behavior of mice in the open field at P16. The motor abilities of
130 both groups were comparable as reflected by the similar distance covered in the arena (GE:
131 2024.81 ± 191.65 cm vs. CON: 2250.34 ± 179.33 cm, $p = 0.24$). All animals spent most of
132 the time in the outer circle of the arena close to the walls and the distance covered in the
133 inner circle was comparable between the groups (CON: 250 ± 48 cm; GE: 278 ± 51 cm).
134 These data suggest that GE mice were not more anxious than CON mice.

135 Taken together, these results indicate that at pre-juvenile age the LEC-dependent
136 associative recognition memory is impaired in GE mice.

137 **The oscillatory entrainment of LEC within prefrontal-hippocampal networks is** 138 **impaired in GE mice throughout development**

139 The behavioral deficits might result from developmental disruption of LEC. To directly
140 address this hypothesis, we investigated the oscillatory and firing activity of LEC and its
141 embedding into PFC-HP networks. For this, we performed multi-site extracellular recordings
142 of local field potential (LFP) and multiple-unit activity (MUA) from LEC, simultaneously with
143 the CA1 area of intermediate/ventral HP (i/vCA1) and prelimbic subdivision (PL) of PFC of
144 urethane-anesthetized P20–23 CON ($n = 16$), GE ($n = 11$) mice *in vivo* (supplementary fig.
145 3). All investigated mice showed similar patterns of continuous network activity, which
146 covered a broad frequencies spectrum and correspond to previously described sleep-like
147 rhythms mimicked by urethane anesthesia^{37, 38, 39}. While the oscillatory power in LEC as well
148 as PFC and HP was comparable in CON and GE mice, the firing activity was significantly
149 increased in both entorhinal layer 5/6 (log firing rate, 1.65 ± 0.18 vs. 0.06 ± 0.65 , $p = 0.04$)
150 and layer 2/3 (log firing rate, 1.74 ± 0.23 vs. -0.20 ± 0.74 , $p = 0.03$) as well as in stratum
151 pyramidale of hippocampal CA1 area (log firing rate, 1.63 ± 0.18 vs. -0.15 ± 0.80 , $p = 0.05$)
152 in GE mice (supplementary fig. 3). The prefrontal firing activity was also increased in GE

153 mice, yet below significance threshold (log firing rate, layer 5/6: 1.16 ± 0.82 vs. 0.28 ± 0.63 ,
154 $p = 0.37$; layer 2/3, 1.40 ± 0.63 vs. 0.43 ± 0.65 , $p = 0.28$).

155 In line with previous studies^{25, 27, 28}, firing deficits at pre-juvenile age might reflect
156 abnormal circuit wiring initiated at earlier stages of development. To test this hypothesis, we
157 investigated the activity patterns within entorhinal-hippocampal-prefrontal networks in
158 neonatal (P8-10) CON ($n = 12$) and GE ($n = 10$) mice (Fig. 2a). Extracellular recordings of
159 LFP and MUA showed that discontinuous spindle-shaped oscillations with frequency
160 components peaking in theta band (4-12 Hz) intermixed with irregular low amplitude beta-
161 gamma band components (12-30 Hz) were the dominant pattern of entorhinal network
162 activity of both groups of mice (Fig. 2a, supplementary fig. 4a). The discontinuous oscillatory
163 events classified as spindle-bursts were superimposed on a slow rhythm (2-4 Hz) that
164 continuously entrained the neonatal LEC (supplementary fig. 4a) and related to respiration⁴⁰.
165 The occurrence and duration of discontinuous oscillatory events (4-30 Hz) were comparable
166 in CON and GE mice (supplementary fig. 4b). However, their power (4-30 Hz) was
167 significantly smaller ($F_{(1,28)} = 11.89$, $p = 0.002$, one-way ANOVA) in GE mice (9.96 ± 1.20)
168 than CON mice (23.45 ± 3.39) (Fig. 2a). Given that single-hit E and G mice were
169 indistinguishable in their activity patterns from CON mice (supplementary fig. 4c), single-hit
170 models were not considered for the rest of investigations. The diminished network activity in
171 LEC was accompanied, as previously reported²⁵, by the dysfunction of network activity in
172 both HP and PFC (Fig. 2b, c).

173 Next, we questioned whether the dampening of oscillatory activity in LEC, HP and
174 PFC during early development related to communication deficits within the limbic networks.
175 For this we firstly assessed the coupling by synchrony between LEC and PFC-HP pathway
176 in neonatal CON ($n = 14$) and GE ($n = 14$) mice by calculating the coherence of oscillatory
177 events and considering only the imaginary part that was not corrupted by volume
178 conductance⁴¹. A tight theta-beta band coupling of spindle-bursts between LEC and HP as
179 well as between HP and PFC was detected in neonatal CON mice (Fig. 2d). In contrast, the
180 imaginary coherence was significantly lower in GE mice (LEC-HP: 0.294 ± 0.015 vs. $0.256 \pm$

181 0.010, $F_{(1, 26)} = 5.18$, $p = 0.03$, one-way ANOVA; HP-PFC: 0.345 ± 0.013 vs. 0.284 ± 0.014 ,
182 $F_{(1, 26)} = 11.340$, $p = 0.002$, one-way ANOVA) (Fig. 2d). The coherence between LEC and
183 PFC was much higher than the coherence calculated for the shuffled data in both CON and
184 GE mice, yet no frequency-specific coupling was detected (Fig. 2d). In a second step, to get
185 better insights into the directionality of information flow within entorhinal-hippocampal-
186 prefrontal networks, we used the generalized partial directed coherence (gPDC), a measure
187 that reflects the directionality of network interactions in different frequency bands. In CON
188 mice, we confirmed the previously reported drive from HP to PFC as well as the stronger
189 information flow from LEC to HP than from LEC to PFC^{32, 42}. The entorhinal drive to HP was
190 significantly decreased in GE mice (0.084 ± 0.006 vs. 0.112 ± 0.006 , $p = 0.0009$, one-way
191 ANOVA), which, besides the previously reported local dysfunction in HP and PFC, might
192 further contribute to the reduction of hippocampal drive to PFC (0.069 ± 0.004 vs. $0.094 \pm$
193 0.006 , $p = 0.002$, one-way ANOVA) (Fig. 2e). The weak drive entorhinal drive to PFC was
194 comparable in CON and GE mice.

195 Taken together, these results uncover the functional pathways of communication
196 within neonatal limbic circuits with the LEC boosting the hippocampal activity and, mainly via
197 hippocampal activation, the PFC activity. Moreover, the data document the entorhinal
198 dysfunction and abnormal coupling within limbic circuits of neonatal GE mice.

199 **Spatially distinct entorhinal projections to HP and PFC are sparser in neonatal GE** 200 **mice**

201 One possible source of dysfunction within entorhinal-hippocampal-prefrontal circuits is the
202 abnormal connectivity between these areas. We previously showed that already at the end
203 of the first postnatal week hippocampal CA1 area strongly innervated the PFC, whereas no
204 direct prefrontal projections targeted the HP. Moreover, we identified projections from LEC to
205 HP as well as PFC in neonatal rats^{25, 42}. However, it is unknown, whether the same or
206 distinct entorhinal populations innervate PFC and HP. To elucidate anatomical integration of
207 LEC within the neonatal HP-PFC pathway, we injected the retrograde tracers CTB555 in HP

208 and CTB488 in PFC of the same P7 mouse ($n = 3$) and monitored the projections after 3
209 days. CTB555 injection confined to i/vCA1 labeled cells mainly in layer 2/3 of LEC (Fig. 3a).
210 CTB488 injection confined to prelimbic-infralimbic subdivisions of the PFC labeled cells in
211 the same layers, yet in a distinct, more superficial part; labeled neurons were detected also
212 in i/vCA1, confirming the previously described hippocampal projection to PFC (Fig. 3a).
213 There was no overlap between the CTB555 and CTB488 labeled neurons in the superficial
214 layers of LEC, indicating that the entorhinal HP- and PFC-projecting neurons had a distinct
215 spatial organization.

216 The substrate of decreased functional coupling within entorhinal-hippocampal-
217 prefrontal networks in GE mice might be the sparser anatomical projections between the
218 three areas in these mice. To test this hypothesis, we quantified the density of entorhinal
219 HP- and PFC-projecting neurons in CON ($n = 4$, 3~4 slices per mouse) and GE mice ($n = 4$,
220 3~4 slices per mouse) (Fig. 3b, c). In line with the prominent entorhinal drive to HP and
221 weaker drive to PFC in CON mice (Fig. 2e), the density of HP-projecting neurons was higher
222 than the density of PFC-projecting neurons (Fig. 3b, c). GE mice showed a significantly ($p =$
223 0.00001) reduced density of HP-projecting neurons (1576.97 ± 80.73) but a similar ($p = 0.92$)
224 density of PFC-projecting neurons (774.66 ± 97.42) when compared with CON mice
225 (2175.75 ± 85.58 , 762.66 ± 87.21) (Fig. 3b, c). To confirm the weaker innervation of HP by
226 LEC axons in GE mice, we injected the anterograde tracer BDA in LEC at P7 and monitored
227 the axonal terminals in HP of CON ($n = 3$) and GE mice ($n = 3$) at P10 (supplementary fig. 5).
228 The high axonal density precluded the quantification of their length; instead, we monitored
229 the intensity of the labeled terminals. GE mice showed a significantly reduced intensity of
230 entorhinal axons in HP, suggesting that sparser projections link the LEC to hippocampal
231 CA1 area in GE mice (supplementary fig. 5c). In contrast, very few BDA-labeled axonal
232 terminals of entorhinal neurons were detected in PFC of both CON and GE mice.

233 Another source of dysfunction within entorhinal-hippocampal-prefrontal circuits in GE
234 mice might represent the LEC neurons *per se* that due to abnormal properties are not able to
235 provide the activation relayed to downstream areas. To test this hypothesis, we performed *in*

236 *in vitro* whole-cell patch-clamp recordings from entorhinal neurons that were either retrogradely
237 labeled by CTB488 / Fluorogold (PFC-projecting neurons), or CTB555 (HP-projecting
238 neurons). The passive membrane properties (RMP, C_m , R_{in} , T_m) of PFC-projecting neurons
239 as well as HP-projecting neurons were similar in P8-10 CON (27 neurons from 10 mice) and
240 GE (12 neurons from 5 mice) mice (Table 1). All investigated neurons showed linear I–V
241 relationships and their firing increased in response to depolarizing current injection. The
242 active membrane properties (i.e. action potential (AP) threshold, AP amplitude, half-width,
243 Rheobase, firing frequency) of both groups of entorhinal neurons did not differ between CON
244 and GE mice (Table 1). These results suggest that circuit dysfunction of GE mice does not
245 mainly relate to cellular abnormalities of entorhinal PFC-projecting and HP-projecting
246 neurons.

247 **Weaker responsiveness of HP to optogenetic activation of LEC in neonatal GE mice**

248 To directly test the functional communication along axonal pathways within entorhinal-
249 hippocampal-prefrontal networks of CON and GE mice, we monitored the responsiveness of
250 the three areas to the activation of LEC. For this, we selectively transfected pyramidal
251 neurons in LEC of CON ($n = 11$) and GE ($n = 13$) mice with a highly efficient fast-kinetics
252 double mutant ChR2E123T/T159C (ET/TC)⁴³ and the red fluorescent protein mCherry by
253 micro-injections performed at P1 (Fig. 4a, supplementary fig. 6).

254 First, we assessed the efficiency of light stimulation in evoking action potentials in
255 entorhinal pyramidal neurons *in vivo*. Blue light pulses (473 nm, 20-40 mW/mm²) at a
256 frequency of 8 Hz led shortly (<10 ms) after the stimulus to precisely timed firing of
257 transfected neurons in the LEC of both P8-10 CON and GE mice (Fig. 4b). The used light
258 power did not cause local tissue heating that might interfere with neuronal spiking^{44, 45}. The
259 efficiency of light stimulation in evoking entorhinal spikes was similar for both CON and GE
260 groups (Fig. 4b). From the second pulse on, the firing of neurons from both groups gradually
261 lost the precise timing to the stimulus and the response reliability, most likely due to the
262 immaturity of entorhinal neurons unable to fire at the set frequency. Ramp light stimulation (3

263 s, 473 nm, 20-40 mW/mm²) induced theta-beta power peaks in the LEC of CON and GE
264 mice (supplementary fig. 7). In line with the unweighted projections from the LEC to the two
265 areas (Fig. 3), pulsed light stimulation in LEC led to rhythmic firing in HP, yet not in PFC (Fig.
266 4b). Quantification of the hippocampal firing probabilities upon stimulus revealed that CA1
267 neurons were reliably activated by light pulses in CON, yet not GE mice (Fig. 4b), most likely
268 due to the reduced number of entorhinal HP-projecting neurons and the sparser entorhinal
269 axonal terminals in HP.

270 Second, to decide whether LEC activation boosts information flow within entorhinal-
271 hippocampal-prefrontal networks, we investigated the synchrony of the three areas upon
272 light stimulation in CON and GE mice. Ramp light stimulation augmented the 10-20 Hz
273 coherence between LEC and HP (0.14 ± 0.05) but not between LEC and PFC (-0.01 ± 0.02)
274 (Fig. 4c). Of note, frequency-specific boosting of HP through LEC activation caused an
275 indirect augmentation of synchrony within prefrontal-hippocampal networks in CON mice
276 (0.19 ± 0.06) (Fig. 4c). In GE mice, the stimulation-induced LEC-HP coherence increase was
277 of lower magnitude (0.04 ± 0.03 vs. 0.14 ± 0.05 , $F_{(1,17)} = 4.10$, $p = 0.049$) and consequently,
278 not sufficient to augment the hippocampal-prefrontal synchrony (-0.03 ± 0.04) (Fig. 4c).

279 Taken together, these results indicate that LEC has a critical role for the activation of
280 HP that on its turn boosts the entrainment of PFC. In contrast, the direct impact of entorhinal
281 activity on PFC is low, if any. The hub function of LEC persists in GE mice, yet the LEC-
282 driven activation of HP is much weaker, being not further relayed to PFC.

283 **The function of entorhinal projections targeting the HP and PFC is selectively** 284 **compromised in neonatal GE mice**

285 To experimentally backup the results above, we monitored the function of entorhinal axonal
286 projections targeting either the PFC or the HP. In all investigated P8-10 mice LEC projected
287 to the prelimbic and infralimbic sub-divisions of PFC, where it mainly targeted layer 5/6
288 neurons (Fig. 5a). Light stimulation (3 ms, 473 nm, 8 Hz) of terminals in PFC of Chr2-
289 transfected entorhinal neurons was performed simultaneously with extracellular LFP and

290 MUA recordings in layer 5/6 of PL (Fig. 5b). Light activation of entorhinal terminals caused a
291 pronounced short-delay (~15 ms) LFP depolarization and augmentation of neuronal firing in
292 PFC of both CON and GE mice. The efficiency of light stimulation in evoking action
293 potentials in layer 5/6 was low and comparable for CON and GE mice (0.19 ± 0.01 vs. $0.18 \pm$
294 0.02). Correspondingly, only 10 out 134 (~7.5%) prefrontal neurons in CON mice and 7 out
295 107 (~7.1%) in GE mice increased their firing upon light stimulation of entorhinal terminals
296 (Fig. 5d).

297 Already at neonatal age, entorhinal projections target the HP (Fig. 3) and, in line with
298 previous studies⁴⁶, accumulate in stratum lacunosum of CA1 area (Fig. 6a). The density of
299 these projections significantly differs between CON and GE mice (Fig. 3, supplementary fig.
300 5). To test the function of entorhinal innervation of HP and whether the sparser projections in
301 GE mice cause the network and neuronal deficits described above, we performed multi-site
302 recordings of LFP and MUA in CA1 area during pulsed and ramp light stimulation of
303 entorhinal terminals in HP (Fig. 6a). The field response evoked by light pulses (3 ms, 473 nm,
304 8 Hz) in HP had a fast (~15 ms) onset in all investigated mice, yet a smaller amplitude
305 ($23.37 \pm 3.91 \mu\text{V}$, $p = 0.040$) in GE mice than CON mice ($50.63 \pm 11.79 \mu\text{V}$) (Fig. 6b). Light
306 stimulation of entorhinal terminals efficiently evoked hippocampal spikes of CON mice
307 (probability 0.72 ± 0.08) (Fig. 6c), which was in line with the dense entorhinal axonal
308 terminals (supplementary fig. 5). The firing probability upon stimulus was significantly ($p =$
309 0.002) lower in the HP of GE mice (0.32 ± 0.05) (Fig. 6c). Not only the firing efficiency
310 decreased but also the number of responsive hippocampal units was lower in GE mice (8
311 out 73, ~11%) when compared to CON mice (22 out of 81, ~27%) (Fig. 6d, e). These results
312 indicate that the function of entorhinal projections in HP is impaired in GE mice, their
313 efficiency to boost the hippocampal activity being decreased.

314 If the function of entorhinal projections to PFC but not to HP is largely intact in GE
315 mice, the question arises, whether the weaker entorhinal drive to HP is still sufficient to
316 entrain the neural activity in PFC. Light activation of entorhinal axonal terminals in HP (Fig.
317 7a) led to an increase of neuronal firing both in layer 5/6 (1.87 ± 0.18) and layer 2/3 ($1.70 \pm$

318 0.16) of PFC in CON mice (Fig. 7b, c). In contrast, the stimulation has a significantly weaker,
319 if any, effect in the PFC of GE mice (layer 5/6, 1.50 ± 0.12 , $p = 0.04$; layer 2/3: 1.44 ± 0.10 , p
320 $= 0.04$). Correspondingly, the prefrontal-hippocampal coupling augmented in CON mice
321 during stimulating entorhinal terminals in HP (relative change 0.09 ± 0.03), yet not in GE
322 mice (relative change, -0.02 ± 0.004 , $p = 0.049$, Fig. 7d).

323 Taken together, these results uncover the pathways of functional wiring within
324 entorhinal-hippocampal-prefrontal circuits and their disruption in GE mice. While the sparse
325 entorhinal projections to PFC seem to be structurally and functionally normal in GE mice, the
326 entorhinal-hippocampal communication is impaired, having indirect effects on the prefrontal
327 activity.

328 DISCUSSION

329 Mouse models mimicking the dual etiology of schizophrenia, such as abnormal DISC1
330 function and immune challenge early in life reproduce the neuronal network and, to a certain
331 amount, behavioral deficits of schizophrenia patients. The origin of these deficits has been
332 hypothesized during development. Indeed, mice of an age corresponding to second-third
333 gestational trimester in humans show prefrontal-hippocampal dysfunction^{25, 27, 28, 29},
334 supporting the hypothesis of developmental miswiring in schizophrenia. The present results
335 uncover novel mechanisms of miswiring in the neonatal brain and highlight the critical role of
336 the LEC as gatekeeper of prefrontal-hippocampal circuits. We show that in mice mimicking
337 the dual genetic-environmental etiology of schizophrenia (i) the patterns of oscillatory activity
338 and coupling within LEC-HP-PFC networks are disrupted already at neonatal age, the
339 entorhinal driving force on HP being particularly reduced, (ii) the substrate of abnormal LEC-
340 HP coupling are sparser entorhinal axonal projections and their poorer efficiency to excite
341 the HP, (iii) the disruption of entorhinal-hippocampal communication is sufficient to decrease
342 the activation of PFC, whereas the direct entorhinal drive to PFC is largely unaffected, and
343 (iv) the associative recognition memory that depends on entorhinal-hippocampal-prefrontal
344 circuits and can be tested already at pre-juvenile age is poor when compared to CON mice.

345 The entorhinal cortex represents a part of medial temporal lobe that is highly
346 interconnected with the hippocampus and subcortical areas, such as the amygdala⁴⁷.
347 Related to its function and input-output connectivity, the entorhinal cortex has been divided
348 into the medial entorhinal cortex (MEC) that is involved in spatial navigation and spatial
349 memory (“Where”)⁴⁸ and LEC that codes context (“What”) and temporal (“When”)
350 information^{49, 50}. In contrast to MEC, the LEC function has been less well dissected. It codes
351 for object features and context-related locations, being critical for the performance in
352 associative recognition memory of adults³⁵. LEC is also involved in olfactory processing, as
353 witnessed by lesions studies of LEC that led to olfactory anterograde amnesia⁵¹ but also
354 facilitation of olfactory recognition⁵². Information transfer through LEC-HP synchrony is
355 critical for olfactory associative learning⁵³. Given the LEC function and its tight embedding
356 into large-scale circuits, it is not surprising that LEC came into the focus when investigating
357 the pathophysiology of major psychiatric illnesses. Clinical, post-mortem and imaging studies
358 identified structural and synaptic deficits in the entorhinal cortex of schizophrenia and bipolar
359 disorder patients^{15, 54, 55, 56}. However, the mechanisms of these deficits remain largely
360 unknown. It has been hypothesized that they result from abnormal development of LEC.

361 The present study addresses this hypothesis and uncovers the functional deficits of
362 LEC embedding into hippocampal-prefrontal circuits during development. Under normal
363 conditions, the neonatal LEC acts as gatekeeper of HP and PFC, facilitating their activation.
364 In line with the density of axonal projections, the direct entorhinal drive to HP is stronger than
365 to PFC. On its turn, the hippocampal activation boosts the firing and oscillatory entrainment
366 of PFC. By these means, two entorhinal pathways, directly and indirectly activate the PFC.
367 They ensure the necessary level of neonatal excitation and oscillatory activation, which are
368 mandatory for adult prefrontal-related behavior⁵⁷. This knowledge gain might be instrumental
369 for answering the question how non-sensory cortices, such as PFC, generate early patterns
370 of oscillatory activity. Spontaneous activity from the periphery travels along axonal
371 projections via brainstem and thalamic nuclei and boosts the entrainment of developing
372 visual, barrel or auditory cortices in oscillatory rhythms that facilitate the emergence of

373 characteristic functional topographies^{58, 59}. Such mechanisms are irrelevant for early
374 prefrontal oscillations; here, it seems that LEC drives the activation patterns. This
375 mechanism is not fully decoupled from sensory inputs, since the LEC receives direct inputs
376 from the olfactory bulb. The blind and deaf mouse pups that do not actively whisker at
377 neonatal age have already adult-like olfactory abilities⁶⁰. The olfactory bulb not only
378 processes and forwards the odor information to the LEC, but also spontaneously generates
379 patterns of early oscillatory activity that activate the LEC^{40, 61}. Therefore, at neonatal age, the
380 entorhinal direct drive to HP as well as direct and indirect to PFC, is controlled by the
381 olfactory system.

382 In mice mimicking the combined genetic and environmental etiology of disease, a
383 prominent dysfunction within neonatal entorhinal-hippocampal-prefrontal networks has been
384 identified. While the direct LEC-PFC communication was largely intact, the entorhinal drive
385 to HP was weaker as result of sparser and reduced efficiency of axonal terminals to excite
386 the hippocampal neurons. The effects of these deficits were detectable also in the
387 downstream area, the PFC. Even if the passive and active membrane properties of
388 entorhinal HP-projecting neurons were largely unaffected in GE mice, the neuronal function
389 was impaired. The origin of this impairment is still unknown. One possible source might
390 represent the dysfunction of local circuits in LEC. The cytoarchitecture of neonatal LEC was
391 normal, yet subtle migration and differentiation deficits cannot be excluded as possible
392 mechanisms, especially when considering that *Disc1* gene represents an intracellular hub of
393 developmental processes. Neurons in deep layers of LEC have abnormal passive and active
394 properties (Rebecca Kringel, *unpublished observations*) that might perturb the intracortical
395 entorhinal connectivity. Another source of entorhinal dysfunction might represent the weaker
396 upstream input as result of olfactory deficits. Robust olfactory deficits have been identified in
397 schizophrenia patients and at-risk youth⁶². The reduced size of the olfactory bulb and the
398 resulting abnormal olfactory processing have been considered as a byproduct of an early
399 developmental disturbance⁶³. Thus, it can be hypothesized that the disturbance of LEC and
400 downstream limbic circuitry involved in memory is, at least in part, the result of an early

401 miswiring of olfactory system. Currently, investigations of olfactory processing of mouse
402 models of disease are lacking. Their achievement might open new perspectives for
403 mechanistic understanding of schizophrenia and in the end, for early diagnostic (i.e.
404 biomarkers) and design of therapeutic strategies.

405 **MATERIALS AND METHODS**

406 **Animal Models.** All experiments were performed in compliance with the German laws and
407 the guidelines of the European Community for the use of animals in research and were
408 approved by the local ethical committee (015/17, 015/18). Timed-pregnant C57BL/6J mice
409 from the animal facility of the University Medical Center Hamburg-Eppendorf were used. The
410 day of vaginal plug detection was defined as gestational day (G) 0.5, whereas the day of
411 birth was defined as postnatal day (P) 0. Multisite extracellular recordings and behavioral
412 testing were performed on pups of both sexes during neonatal development (i.e. P8-P10) as
413 well as during pre-juvenile development (i.e. P16-P23). Heterozygous genetically engineered
414 mutant DISC1 mice carrying a *Disc1* allele (Disc1Tm1Kara) on a C57BL6/J background
415 were used. Due to two termination codons and a premature polyadenylation site, the allele
416 produces a truncated transcript⁶⁴. Genotypes were determined using genomic DNA and
417 following primer sequences: forward primer 5'-TAGCCACTCTCATTGTCAGC-3', reverse
418 primer 5'-CCTCATCCCTTCCACTCAGC-3'. Mutant DISC1 mice were challenged by MIA,
419 using the viral mimetic poly I:C (5mg/kg) injected intravenously (i.v.) into the pregnant dams
420 at gestational day G9.5. The resulting offspring mimicking the dual genetic-environmental
421 etiology of mental disorders were classified as GE mice (DISC1 knock-down + MIA). The
422 offspring of wild-type C57BL/6J dams injected at G9.5 with saline (0.9%, i.v.) were classified
423 as CON mice (control).

424 **Electrophysiological recordings in vivo.** For neonatal recordings in non-anesthetized
425 state, 0.5% bupivacain / 1% lidocaine was locally applied on the neck muscles. For pre-
426 juvenile recordings under anesthesia, mice were injected intraperitoneally (i.p.) with urethane
427 (1 mg/g body weight; Sigma-Aldrich, MO, USA) prior to surgery. For both age groups, under

428 isoflurane anesthesia (induction: 5%, maintenance: 2.5%) the head of the pup was fixed into
429 a stereotaxic apparatus using two plastic bars mounted on the nasal and occipital bones with
430 dental cement. The bone above the PFC (0.5 mm anterior to bregma, 0.1-0.5 mm right to the
431 midline), hippocampus (3.5 mm posterior to bregma, 3.5 mm right to the midline), LEC (4
432 mm posterior to bregma, 6 mm right to the midline) was carefully removed by drilling a hole
433 of <0.5 mm in diameter. After a 10 min recovery period on a heating blanket, mouse was
434 placed into the setup for electrophysiological recording. Throughout the surgery and
435 recording session the mouse was positioned on a heating pad with the temperature kept at
436 37°C.

437 A four-shank optoelectrode (NeuroNexus, MI, USA) containing 4x4 recording sites
438 (0.4-0.8 MΩ impedance, 100 μm spacing, 125 μm intershank spacing) was inserted into the
439 PL of PFC. A one-shank optoelectrode (NeuroNexus, MI, USA) containing 1x16 recordings
440 sites (0.4-0.8 MΩ impedance, 50 μm spacing) was inserted into CA1 area. A one-shank
441 optoelectrode (NeuroNexus, MI, USA) containing 1x16 recordings sites (0.4-0.8 MΩ
442 impedance, 100 μm spacing) was inserted into LEC horizontally. An optical fiber ending 200
443 μm above the top recording site aligned with each recording shank. A silver wire was
444 inserted into the cerebellum and served as ground and reference electrode. Extracellular
445 signals were band-pass filtered (0.1-9,000 Hz) and digitized (32 kHz) with a multichannel
446 extracellular amplifier (Digital Lynx SX; Neuralynx, Bozeman, MO, USA) and the Cheetah
447 acquisition software (Neuralynx). Spontaneous (i.e. not induced by light stimulation) activity
448 was recorded for 20 min at the beginning of each recording session as baseline activity. The
449 position of recording electrodes in the PL, CA1 area of i/vHP and LEC was confirmed post
450 mortem. Wide field fluorescence images were acquired to reconstruct the recording
451 electrode position in brain slices of electrophysiologically investigated pups. Only pups with
452 correct electrode position were considered for further analysis. In PL, the most medial shank
453 was inserted to target layer 2/3, whereas the most lateral shank was located into layer 5/6.
454 For the analysis of hippocampal LFP, the recording site located in the pyramidal layer, where
455 SPWs reverse⁶⁵ was selected to minimize any non-stationary effects of large amplitude

456 events. For the analysis of LEC LFP, the recording site that 700 μm above the pyramidal
457 layer of CA1 was selected.

458 ***Viral transfection in pyramidal neurons of LEC and light stimulation.*** Transfection of
459 pyramidal neurons with a ChR2 derivative was achieved by injecting 0.1 μl of the construct
460 (AAV9-CaMKII-ChR2(E123T/T159C)-mCherry, at a titer $> 1 \times 10^{13}$ vg/mL, Addgene,
461 Watertown, MA, USA) in LEC on the right hemisphere of P0–1 pups. The pups were placed
462 in a stereotactic apparatus and kept under anesthesia with isoflurane (induction: 5%,
463 maintenance: 2.5%) for the entire procedure. A 10 mm incision of the skin on the head was
464 performed with small scissors. The bone above the LEC was carefully removed using a
465 syringe. The injection was achieved via a 10 μl microsyringe pump controller. The injection
466 speed (0.05 $\mu\text{l}/\text{min}$) was slow with the maintenance of the syringe in place for at least 8 min.
467 Pulsatile (laser on-off, pulse 3 ms-long, 8 Hz, 3 s-long) or ramp (linearly increasing power, 3
468 s-long) light stimulations were performed with an arduino uno (Arduino, Italy) controlled
469 diode laser (473 nm; Omicron, Austria). Laser power was adjusted to trigger neuronal
470 spiking in response to $>25\%$ of 3 ms-long light pulses at 8 Hz. Resulting light power was in
471 the range of 20-40 mW/mm^2 at the fiber tip.

472 ***In vitro whole-cell patch-clamp recordings.*** Whole-cell patch-clamp recordings were
473 performed from neurons identified by their location in the LEC and their projections to PFC
474 (CTB488 / Fluorogold retrograde-labeled neurons) or HP (CTB555 retrograde-labeled
475 neurons). All recordings were performed at room temperature. Recording electrodes (5–
476 8M Ω) were filled with K-gluconate based solution containing (in mM):130 K-gluconate, 10
477 Hepes, 0.5 EGTA, 4Mg-ATP, 0.3Na-GTP, 8 NaCl (285 mosmol kg-1H₂O, pH 7.4) and 0.5%
478 biocytin for post hoc morphological identification of recorded cells. Capacitance artefacts
479 were minimized using the built-in circuitry of the patch-clamp amplifier (HEKA EPC 10,
480 HEKA Elektronik, Germany). The signals were low-pass filtered at 10 kHz and recorded
481 online. All potentials were corrected for the liquid junction potential of the gluconate-based
482 electrode solution, which, according to own measurement, was -8.65 mV. The resting

483 membrane potential (RMP) was measured immediately after obtaining the whole-cell
484 configuration. For the determination of input resistance (R_{in}), membrane time constant (T_m)
485 and membrane capacitance (C_m), hyper-polarizing current pulses (-60 pA) of 600 ms in
486 duration were applied from the resting membrane potential. Firing frequency was assessed
487 at a depolarizing current pulse of 100 pA at the same length of 600 ms. Analysis was
488 performed offline using custom-written scripts in the MATLAB environment.

489 **Behavioral protocols.** The exploratory behavior and recognition memory of CON and GE
490 mice were tested at pre-juvenile age using previously established experimental protocols⁶⁶.
491 Briefly, all behavioral tests were conducted in a custom-made circular white arena, the size
492 of which (D: 34 cm, H: 30 cm) maximized exploratory behavior, while minimizing incidental
493 contact with testing objects⁶⁷. The objects used for testing of associative recognition were six
494 differently shaped, textured and colored, easy to clean items that were provided with
495 magnets to fix them to the bottom of the arena. Object sizes (H: 3 cm, diameter: 1.5-3 cm)
496 were smaller than twice the size of the mouse and did not resemble living stimuli (no eye
497 spots, predator shape). The objects were positioned at 10 cm from the borders and 8 cm
498 from the center of the arena. After every trial the objects and arena were cleaned with 0.1 %
499 acetic acid to remove all odors. A black and white CCD camera (VIDEOR TECHNICAL E.
500 Hartig GmbH, Roedermark, Germany) was mounted 100 cm above the arena and connected
501 to a PC via PCI interface serving as frame grabber for video tracking software (Video Mot2
502 software, TSE Systems GmbH, Bad Homburg, Germany).

503 **Exploratory behavior in the open field.** Pre-juvenile mice (P16) were allowed to freely
504 explore the testing arena for 10 min. Additionally, the floor area of the arena was digitally
505 subdivided in 8 zones (4 center zones and 4 border zones) using the zone monitor mode of
506 the VideoMot 2 analysis software (VideoMot 2, TSE Systems GmbH). The time spent by
507 pups in center and border zones, as well as the running distance and velocity was quantified.

508 **Novel object preference (distinct objects) (NOPd) and object-location preference (OLP)**
509 **tasks.** All protocols for assessing associative recognition memory in P17 (NOPd) and P18

510 (OLP) mice consisted of familiarization and test trials. During the familiarization trial each
511 mouse was placed into the arena containing two different objects and released with the back
512 to the objects. After 10 min of free exploration of objects the mouse was returned to a
513 temporary holding cage. Subsequently, the test trial was performed after a delay of 5 min
514 post-familiarization. In NOPd task, the mice were allowed to investigate one familiar and one
515 novel object with a different shape and texture for 5 min. The nature of this test is similar to
516 the novel object preference test, except that the test trial involves an association between
517 two different objects (an association of object-object). In OLP task, the mice were allowed to
518 investigate one familiar and a copy of the old object that was previously presented for 5 min.
519 This test examines whether animals recognize the location that was once occupied by a
520 particular object (an association of object-location). Object interaction during the first 4 min
521 was analyzed and compared between the groups. All trials were video-tracked and the
522 analysis was performed using the Video Mot2 analysis software. The object recognition
523 module of the software was used and a 3-point tracking method identified the head, the rear
524 end and the center of gravity of the mouse. Digitally, a circular zone of 1.5 cm was created
525 around each object and every entry of the head point into this area was considered as object
526 interaction. Climbing or sitting on the object, mirrored by the presence of both head and
527 center of gravity points within the circular zone, were not counted as interactions.

528 The object discrimination was computed for NOPd and OLP as $(\text{time at object2} - \text{time at}$
529 $\text{object1}) / (\text{time at object1} + \text{time at object2})$ (Fig. 1).

530 ***Behavioral protocols for quantifying the cFos expression in mouse doing NOPd or***
531 ***OLP task.*** P16 CON mice were randomly divided into 2 groups (n = 4 mice / group). The
532 mice were allowed to freely explore the arena containing two different objects for 10 mins.
533 This familiarization process continued for 3 days with 2 trials per day. On the third day (P18),
534 5 mins after the last familiarization trial, 3 mice from one group were signed to perform the
535 test trial (5 mins) of NOPd task, whereas one mouse to perform the familiarization trial.
536 Similarly, for the other group, 3 mice were assigned to perform the test trial (5 mins) of OLP

537 task and one mouse to perform the familiarization trial. The mice were perfused ~90 min
538 after the last behavioral trial.

539 **Retrograde tracing.** For retrograde tracing, P7 mice received retrograde tracer CTB555
540 (Cholera Toxin Subunit B, Alexa Fluor 455 Conjugate) injections into HP (0.7mm anterior
541 from the lambda, 2.4 mm from midline, 1.6 mm depth), and CTB488 (Cholera Toxin Subunit
542 B, Alexa Fluor 488 Conjugate) injections into PFC (0.7mm anterior from to bregma, 0.1 mm
543 from midline, 1.9 mm depth). The pups were placed in a stereotactic apparatus and kept
544 under anesthesia with isoflurane (induction: 5%, maintenance: 2.5%) for the entire
545 procedure. A 10 mm incision of the skin on the head was performed with small scissors. The
546 bone above the HP and PFC was carefully removed using a syringe. A total volume of 0.1 μ l
547 of CTB (2.5% in PBS) was delivered via a 10 μ l microsyringe pump controller into PFC or
548 HP. The slow injection speed (0.05 μ l/min) and the maintenance of the syringe in place for at
549 least 8 min ensured an optimal diffusion of the tracer. The pups were perfused at P10.

550 **Anterograde tracing.** Two anterograde tracers were used. First, to quantify the axonal
551 terminals from LEC to HP, anterograde tracer biotinylated dextran amine (BDA) (Thermo
552 Fisher Scientific, USA) was used. Mice were injected at P7 with BDA unilaterally into LEC
553 using iontophoresis. The bone above LEC was carefully removed using a syringe. A glass
554 capillary (~30 μ m tip diameter) was filled with ~1 μ L of 5% BDA diluted in 0.125 M
555 phosphate buffer by capillary forces, and a silver wire was inserted such that it was in
556 contact with the BDA solution. The positive pole of the iontophoresis device was attached to
557 the silver wire, the negative one was attached to the skin of the neck. Iontophoretically
558 injection by applying anodal current to the pipette (6 s on/off current pulses of 6 μ A) was
559 done for 10 min. Following injection, the pipette was left in place for at least 5 min and then
560 slowly retracted. The scalp was closed by application of tissue adhesive glue and the pups
561 were left on a heating pad for 10–15 min to fully recover before they were given back to the
562 mother. The pups were perfused at P10. Second, to locate the innervated neurons in PFC by
563 LEC, anterograde trans-synaptic tracer wheat germ agglutinin (WGA) (Thermo Fisher

564 Scientific, USA) was used. Mice were injected at P8 with WGA unilaterally into LEC. A total
565 volume of 0.1 μ l of WGA (2.5% in PBS) was delivered via a 10 μ l microsyringe pump
566 controller. The slow injection speed (0.05 μ l/min) and the maintenance of the syringe in
567 place for at least 8 min ensured an optimal diffusion of the tracer. 40 hours after the injection,
568 the pups were perfused.

569 **Histology and staining protocols.** Histological procedures were performed as previously
570 described^{26, 27}. Briefly, P8-10 and P18-23 mice were anesthetized with 10% ketamine
571 (aniMedica) / 2% xylazine (WDT) in 0.9% NaCl solution (10 μ g/g body weight, i.p.) and
572 transcardially perfused with Histofix (Carl Roth) containing 4% paraformaldehyde. Brains
573 were postfixed in Histofix for 24 h and sectioned coronally at 50 μ m (immunohistochemistry)
574 or 100 μ m (quantification for CTB labeled neurons). Free-floating slices were permeabilized
575 and blocked with PBS containing 0.8 % Triton X 100 (Sigma-Aldrich, MO, USA), 5% normal
576 bovine serum (Jackson Immuno Research, PA, USA) and 0.05% sodium azide. For cFos
577 staining, slices were incubated with mouse monoclonal Alexa Fluor-555 conjugated antibody
578 against cFos (1:200, MAB377X, Merck Millipore, MA, USA), followed by 2h incubation with
579 Alexa Fluor-488 goat anti-rabbit IgG secondary antibody (1:500, A11008, Merck Millipore,
580 MA). For BDA staining, slices were incubated with streptavidin (Cy3, 1:500, ThermoFisher).
581 For WGA staining, slices were incubated with goat anti-WGA IgG (1:500), followed by 2h
582 incubation with Alexa Fluor-488 goat anti-rabbit IgG secondary antibody (1:500, A11008,
583 Merck Millipore, MA). Slices were transferred to glass slides and covered with Fluoromount
584 (Sigma-Aldrich, MO, USA). Wide-field fluorescence images were acquired to reconstruct the
585 recording electrode position.

586 **Quantification of cFos, CTB488, CTB555, WGA labeled neurons.** All quantifications were
587 carried out blind to the experimental condition. Using a light microscope, photographs of the
588 relevant areas (LEC for cFos, CTB488, CTB555; PFC for WGA) were taken with a
589 consistent light level (Olympus FX-100). 3~4 slices per animal were used. Images were
590 processed using ImageJ software. The number of cFos positive neurons, CTB488 positive

591 neurons, CTB555 positive neurons and WGA positive neurons were counted manually in the
592 interested regions.

593 **Quantification of BDA-labeled axonal terminals.** High magnification images were
594 acquired by confocal microscopy (DM IRBE, Leica Microsystems, Zeiss LSN700) from
595 stratum lacunosum-moleculare of CA1 to quantify LEC axonal terminals labeled by BDA.
596 Microscopic stacks were acquired as 2048×2048 pixel images (pixel size, 78 nm; Z-step,
597 500 nm). All images were similarly processed and analyzed using ImageJ software.

598 **Data Analysis.** Data were imported and analyzed offline using custom-written tools in
599 Matlab software version 7.7 (Mathworks). The data were processed as following: (i) band-
600 pass filtered (500-5000 Hz) to detect MUA as negative deflections exceeding five times the
601 standard deviation of the filtered signals and (ii) low-pass filtered (<1500 Hz) using a third
602 order Butterworth filter before downsampling to 1000 Hz to analyze the LFP. All filtering
603 procedures were performed in a phase-preserving manner. The position of Dil-stained
604 recording electrodes in PL (most medial shank confined to layer 2/3, most temporal shank
605 confined to layer 5/6), CA1 and LEC was confirmed post-mortem by histological evaluation.
606 Additionally, electrophysiological features (i.e. reversal of LFP and high MUA frequency over
607 stratum pyramidale of CA1) were used for confirmation of the exact recording position in HP.

608 **Detection of neonatal oscillatory activity.** Discontinuous oscillatory events were detected
609 using a previously developed unsupervised algorithm⁶⁸ and confirmed by visual inspection.
610 Briefly, deflections of the root-mean-square of band-pass (3-100 Hz) filtered signals
611 exceeding a variance-dependent threshold were assigned as network oscillations. The
612 threshold was determined by a Gaussian fit to the values ranging from 0 to the global
613 maximum of the root-mean-square histogram. Only oscillatory events >1 s were considered
614 for further analysis. Time-frequency plots were calculated by transforming the data using the
615 Morlet continuous wavelet.

616 **Power spectral density.** For power spectral density analysis, 1 s-long window of network
617 oscillations were concatenated and the power was calculated using Welch's method with

618 non-overlapping windows. For optical stimulation, we compared the average power during
 619 the 1.5 s-long time window preceding the stimulation to the last 1.5 s-long time window of
 620 light-evoked activity.

621 **Single unit activity (SUA).** SUA was detected and clustered using klusta (Rossant et al.,
 622 2016) and manually curated using phy (<https://github.com/cortex-lab/phy>). Data were
 623 imported and analyzed using custom-written tools in the MATLAB. Spikes occurring in a 20
 624 ms-long time window after the start of a light pulse were considered to be light-evoked.
 625 Stimulation efficacy was calculated as the probability of at least one spike occurring in this
 626 period.

627 **Firing rate.** The firing rate was computed by dividing the total number of spikes by the
 628 duration of the analyzed time window.

629 **Spectral coherence.** Coherence was calculated using the coherence method. Briefly, the
 630 coherence was calculated (using the functions *cpsd.m* and *pwelch.m*) by cross-spectral
 631 density between the two signals and normalized by the power spectral density of each. The
 632 computation of the coherence C over frequency (f) for the power spectral density P of signal
 633 X and Y was performed according to the formula:

$$C_{XY}(f) = \left| \left(\frac{P_{XY}(f)}{\sqrt{P_{XX}(f)P_{YY}(f)}} \right) \right|$$

634 **Directionality methods.** To investigate the directionality of functional connectivity between
 635 PFC and HP, gPDC was used. gPDC is based on linear Granger causality measure in the
 636 frequency domain. The method attempts to describe the causal relationship between
 637 multivariate time series based on the decomposition of multivariate partial coherence
 638 computed from multivariate autoregressive models. The LFP signal was divided into 1s-long
 639 segments containing the oscillatory activity. After de-noising using Matlab wavelet toolbox,
 640 gPDC was calculated using a previously described algorithm^{69, 70}.

641 **Estimation of light propagation.** The spatial pattern of light propagation *in vivo* was
642 estimated using a previously developed model⁴⁵ based on Monte Carlo simulation (probe
643 parameters: light fiber diameter: 50 μm , numerical aperture: 0.22, light parameters: 594 nm,
644 0.6 mW).

645 **Statistical analysis.** Statistical analyses were performed in Matlab environment. Significant
646 differences were detected by paired t-test or one-way ANOVA. Investigators were blinded to
647 the group allocation when the quantifications of cFos expression, CTB488 and CTB555
648 positive neurons in LEC, and WGA positive neurons in PFC were performed. Data are
649 presented as mean \pm sem. Significance levels of $p < 0.05$ (*), $p < 0.01$ (**) or $p < 0.001$ (***)
650 were tested. Statistical parameters can be found in the main text.

651 **Code availability**

652 All the codes used in the current study are available from the corresponding author upon
653 request.

654 **Data availability**

655 The data supporting the findings of this study is available with the article and its
656 Supplementary Information file, or is available from the corresponding author upon request.

657 **References**

- 658 1. van Os J, Kenis G, Rutten BPF. The environment and schizophrenia. *Nature* **468**,
659 203-212 (2010).
- 660 2. Howes OD, Murray RM. Schizophrenia: an integrated sociodevelopmental-cognitive
661 model. *Lancet* **383**, 1677-1687 (2014).
- 662 3. Goldberg AD, Allis CD, Bernstein E. Epigenetics: A Landscape Takes Shape. *Cell*
663 **128**, 635-638 (2007).
- 664 4. Meyer-Lindenberg A, *et al.* Neural correlates of genetically abnormal social cognition
665 in Williams syndrome. *Nat Neurosci* **8**, 991-993 (2005).
- 666 5. Bähner F, Meyer-Lindenberg A. Hippocampal–prefrontal connectivity as a
667 translational phenotype for schizophrenia. *Eur Neuropsychopharmacol* **27**, 93-106
668 (2017).
- 669 6. Rasetti R, Sambataro F, Chen Q, Callicott JH, Mattay VS, Weinberger DR. Altered
670 Cortical Network Dynamics: A Potential Intermediate Phenotype for Schizophrenia
671 and Association With ZNF804A. *Arch Gen Psychiatry* **68**, 1207-1217 (2011).
- 672 7. Meyer-Lindenberg A. From maps to mechanisms through neuroimaging of
673 schizophrenia. *Nature* **468**, 194-202 (2010).
- 674 8. Kupferschmidt DA, Gordon JA. The dynamics of disordered dialogue: Prefrontal,
675 hippocampal and thalamic miscommunication underlying working memory deficits in
676 schizophrenia. *BNA* **2**, 2398212818771821 (2018).
- 677 9. Nilssen ES, Doan TP, Nigro MJ, Ohara S, Witter MP. Neurons and networks in the
678 entorhinal cortex: A reappraisal of the lateral and medial entorhinal subdivisions
679 mediating parallel cortical pathways. *Hippocampus* **29**, 1238-1254 (2019).
- 680 10. Arnold PJ. Dimensional Standardization and Production Scale in Mesoamerican
681 Ceramics. *Lat Am Antiq* **2**, 363-370 (1991).
- 682 11. Arnold SE. Cellular and Molecular Neuropathology of the Parahippocampal Region in
683 Schizophrenia. *Ann N Y Acad Sci* **911**, 275-292 (2000).
- 684 12. Baiano M, *et al.* Decreased entorhinal cortex volumes in schizophrenia. *Schizophr*
685 *Res* **102**, 171-180 (2008).
- 686 13. Akil M, Lewis DA. Cytoarchitecture of the entorhinal cortex in schizophrenia. *Am J*
687 *Psychiatry* **154**, 1010-1012 (1997).
- 688 14. Hemby SE, Ginsberg SD, Brunk B, Arnold SE, Trojanowski JQ, Eberwine JH. Gene
689 Expression Profile for Schizophrenia: Discrete Neuron Transcription Patterns in the
690 Entorhinal Cortex. *Arch Gen Psychiatry* **59**, 631-640 (2002).

- 691 15. Falkai P, Schneider-Axmann T, Honer WG. Entorhinal cortex pre-alpha cell clusters
692 in schizophrenia: quantitative evidence of a developmental abnormality. *Biol*
693 *Psychiatry* **47**, 937-943 (2000).
- 694 16. Bolkan SS, *et al.* Thalamic projections sustain prefrontal activity during working
695 memory maintenance. *Nat Neurosci* **20**, 987-996 (2017).
- 696 17. Parnaudeau S, *et al.* Inhibition of Mediodorsal Thalamus Disrupts Thalamofrontal
697 Connectivity and Cognition. *Neuron* **77**, 1151-1162 (2013).
- 698 18. Chun S, *et al.* Specific disruption of thalamic inputs to the auditory cortex in
699 schizophrenia models. *Science* **344**, 1178-1182 (2014).
- 700 19. Insel TR. Rethinking schizophrenia. *Nature* **468**, 187-193 (2010).
- 701 20. Sumiyoshi T, *et al.* Enhanced locomotor activity in rats with excitotoxic lesions of the
702 entorhinal cortex, a neurodevelopmental animal model of schizophrenia: Behavioral
703 and in vivo microdialysis studies. *Neurosci Lett* **364**, 124-129 (2004).
- 704 21. Meyer F, Peterschmitt Y, Louilot A. Postnatal functional inactivation of the entorhinal
705 cortex or ventral subiculum has different consequences for latent inhibition-related
706 striatal dopaminergic responses in adult rats. *Eur J Neurosci* **29**, 2035-2048 (2009).
- 707 22. Fell J, *et al.* Human memory formation is accompanied by rhinal–hippocampal
708 coupling and decoupling. *Nat Neurosci* **4**, 1259-1264 (2001).
- 709 23. Cunningham MO, *et al.* Region-Specific Reduction in Entorhinal Gamma Oscillations
710 and Parvalbumin-Immunoreactive Neurons in Animal Models of Psychiatric Illness. *J*
711 *Neurosci* **26**, 2767 (2006).
- 712 24. Brandon NJ, Sawa A. Linking neurodevelopmental and synaptic theories of mental
713 illness through DISC1. *Nat Rev Neurosci* **12**, 707-722 (2011).
- 714 25. Hartung H, *et al.* From Shortage to Surge: A Developmental Switch in Hippocampal–
715 Prefrontal Coupling in a Gene–Environment Model of Neuropsychiatric Disorders.
716 *Cereb Cortex* **26**, 4265-4281 (2016).
- 717 26. Oberlander VC, Xu X, Chini M, Hanganu-Opatz IL. Developmental dysfunction of
718 prefrontal–hippocampal networks in mouse models of mental illness. *Eur J Neurosci*
719 **50**, 3072-3084 (2019).
- 720 27. Xu X, Chini M, Bitzenhofer SH, Hanganu-Opatz IL. Transient Knock-Down of
721 Prefrontal DISC1 in Immune-Challenged Mice Causes Abnormal Long-Range
722 Coupling and Cognitive Dysfunction throughout Development. *J Neurosci* **39**, 1222
723 (2019).
- 724 28. Xu X, Song L, Hanganu-Opatz IL. Knock-Down of Hippocampal DISC1 in Immune-
725 Challenged Mice Impairs the Prefrontal–Hippocampal Coupling and the Cognitive
726 Performance Throughout Development. *Cereb Cortex* **31**, 1240-1258 (2021).

- 727 29. Chini M, *et al.* Resolving and Rescuing Developmental Miswiring in a Mouse Model
728 of Cognitive Impairment. *Neuron* **105**, 60-74.e67 (2020).
- 729 30. Comer AL, *et al.* Increased expression of schizophrenia-associated gene C4 leads to
730 hypoconnectivity of prefrontal cortex and reduced social interaction. *PLoS Biol* **18**,
731 e3000604 (2020).
- 732 31. Jones BF, Witter MP. Cingulate cortex projections to the parahippocampal region
733 and hippocampal formation in the rat. *Hippocampus* **17**, 957-976 (2007).
- 734 32. Hartung H, Brockmann MD, Pöschel B, De Feo V, Hanganu-Opatz IL. Thalamic and
735 Entorhinal Network Activity Differently Modulates the Functional Development of
736 Prefrontal–Hippocampal Interactions. *J Neurosci* **36**, 3676 (2016).
- 737 33. Mathew I, *et al.* Medial Temporal Lobe Structures and Hippocampal Subfields in
738 Psychotic Disorders: Findings From the Bipolar-Schizophrenia Network on
739 Intermediate Phenotypes (B-SNIP) Study. *JAMA Psychiatry* **71**, 769-777 (2014).
- 740 34. Staresina BP, Reber TP, Niediek J, Boström J, Elger CE, Mormann F. Recollection in
741 the human hippocampal-entorhinal cell circuitry. *Nat Commun* **10**, 1503 (2019).
- 742 35. Wilson DIG, Watanabe S, Milner H, Ainge JA. Lateral entorhinal cortex is necessary
743 for associative but not nonassociative recognition memory. *Hippocampus* **23**, 1280-
744 1290 (2013).
- 745 36. Krüger H-S, Brockmann MD, Salamon J, Ittrich H, Hanganu-Opatz IL. Neonatal
746 hippocampal lesion alters the functional maturation of the prefrontal cortex and the
747 early cognitive development in pre-juvenile rats. *Neurobiol Learn Mem* **97**, 470-481
748 (2012).
- 749 37. Wolansky T, Clement EA, Peters SR, Palczak MA, Dickson CT. Hippocampal Slow
750 Oscillation: A Novel EEG State and Its Coordination with Ongoing Neocortical Activity.
751 *J Neurosci* **26**, 6213 (2006).
- 752 38. Clement EA, Richard A, Thwaites M, Ailon J, Peters S, Dickson CT. Cyclic and
753 Sleep-Like Spontaneous Alternations of Brain State Under Urethane Anaesthesia.
754 *PLOS ONE* **3**, e2004 (2008).
- 755 39. Pagliardini S, Gosgnach S, Dickson CT. Spontaneous Sleep-Like Brain State
756 Alternations and Breathing Characteristics in Urethane Anesthetized Mice. *PLOS*
757 *ONE* **8**, e70411 (2013).
- 758 40. Gretenkord S, *et al.* Coordinated electrical activity in the olfactory bulb gates the
759 oscillatory entrainment of entorhinal networks in neonatal mice. *PLoS Biol* **17**,
760 e2006994 (2019).
- 761 41. Nolte G, Bai O, Wheaton L, Mari Z, Vorbach S, Hallett M. Identifying true brain
762 interaction from EEG data using the imaginary part of coherency. *Clin Neurophysiol*
763 **115**, 2292-2307 (2004).

- 764 42. Brockmann Marco D, Pöschel B, Cichon N, Hanganu-Opatz Ileana L. Coupled
765 Oscillations Mediate Directed Interactions between Prefrontal Cortex and
766 Hippocampus of the Neonatal Rat. *Neuron* **71**, 332-347 (2011).
- 767 43. Berndt A, *et al.* High-efficiency channelrhodopsins for fast neuronal stimulation at low
768 light levels. *PNAS* **108**, 7595-7600 (2011).
- 769 44. Bitzenhofer SH, Ahlbeck J, Hanganu-Opatz IL. Methodological Approach for
770 Optogenetic Manipulation of Neonatal Neuronal Networks. *Front Cell Neurosci* **11**,
771 239 (2017).
- 772 45. Stujenske JM, Spellman T, Gordon JA. Modeling the Spatiotemporal Dynamics of
773 Light and Heat Propagation for In Vivo Optogenetics. *Cell Rep* **12**, 525-534 (2015).
- 774 46. Kitamura T, Macdonald CJ, Tonegawa S. Entorhinal-hippocampal neuronal circuits
775 bridge temporally discontinuous events. *Learn Mem* **22**, 438-443 (2015).
- 776 47. Witter MP, Wouterlood FG, Naber PA, Van Haeften T. Anatomical Organization of
777 the Parahippocampal-Hippocampal Network. *Ann N Y Acad Sci* **911**, 1-24 (2000).
- 778 48. Moser EI, Moser M-B, McNaughton BL. Spatial representation in the hippocampal
779 formation: a history. *Nat Neurosci* **20**, 1448-1464 (2017).
- 780 49. Tsao A, *et al.* Integrating time from experience in the lateral entorhinal cortex. *Nature*
781 **561**, 57-62 (2018).
- 782 50. Wang C, *et al.* Egocentric coding of external items in the lateral entorhinal cortex.
783 *Science* **362**, 945-949 (2018).
- 784 51. Staubli U, Fraser D, Kessler M, Lynch G. Studies on retrograde and anterograde
785 amnesia of olfactory memory after denervation of the hippocampus by entorhinal
786 cortex lesions. *Behav Neural Biol* **46**, 432-444 (1986).
- 787 52. Wirth S, Ferry B, Di Scala G. Facilitation of olfactory recognition by lateral entorhinal
788 cortex lesion in rats. *Behav Brain Res* **91**, 49-59 (1998).
- 789 53. Igarashi KM, Lu L, Colgin LL, Moser M-B, Moser EI. Coordination of entorhinal–
790 hippocampal ensemble activity during associative learning. *Nature* **510**, 143-147
791 (2014).
- 792 54. Bachus SE, Hyde TM, Herman MM, Egan MF, Kleinman JE. Abnormal
793 cholecystinin mRNA levels in entorhinal cortex of schizophrenics. *J Psychiatr Res*
794 **31**, 233-256 (1997).
- 795 55. Benes FM, Berretta S. GABAergic Interneurons: Implications for Understanding
796 Schizophrenia and Bipolar Disorder. *Neuropsychopharmacology* **25**, 1-27 (2001).
- 797 56. Pantazopoulos H, Lange N, Baldessarini RJ, Berretta S. Parvalbumin Neurons in the
798 Entorhinal Cortex of Subjects Diagnosed With Bipolar Disorder or Schizophrenia. *Biol*
799 *Psychiatry* **61**, 640-652 (2007).

- 800 57. Bitzenhofer SH, Pöppel JA, Chini M, Marquardt A, Hanganu-Opatz IL. Transient
801 developmental increase of prefrontal activity alters network maturation and causes
802 cognitive dysfunction in adult mice. *Neuron, in press*, (2020).
- 803 58. Khazipov R, Sirota A, Leinekugel X, Holmes GL, Ben-Ari Y, Buzsáki G. Early motor
804 activity drives spindle bursts in the developing somatosensory cortex. *Nature* **432**,
805 758-761 (2004).
- 806 59. Hanganu IL, Ben-Ari Y, Khazipov R. Retinal Waves Trigger Spindle Bursts in the
807 Neonatal Rat Visual Cortex. *J Neurosci* **26**, 6728 (2006).
- 808 60. Welker W. Analysis of Sniffing of the Albino Rat. *Behaviour* **22**, 223-224 (1964).
- 809 61. Kostka JK, Gretenkord S, Spehr M, Hanganu-Opatz IL. Bursting mitral cells time the
810 oscillatory coupling between olfactory bulb and entorhinal networks in neonatal mice.
811 *J Physiol* **598**, 5753-5769 (2020).
- 812 62. Moberg PJ, *et al.* Meta-Analysis of Olfactory Function in Schizophrenia, First-Degree
813 Family Members, and Youths At-Risk for Psychosis. *Schizophr Bull* **40**, 50-59 (2014).
- 814 63. Turetsky BI, *et al.* Structural anomalies of the peripheral olfactory system in
815 psychosis high-risk subjects. *Schizophr Res* **195**, 197-205 (2018).
- 816 64. Kvajo M, *et al.* A mutation in mouse *Disc1* that models a schizophrenia risk allele
817 leads to specific alterations in neuronal architecture and cognition. *PNAS* **105**, 7076-
818 7081 (2008).
- 819 65. Bitzenhofer SH, Hanganu-Opatz IL. Oscillatory coupling within neonatal prefrontal-
820 hippocampal networks is independent of selective removal of GABAergic neurons in
821 the hippocampus. *Neuropharmacology* **77**, 57-67 (2014).
- 822 66. Kruger HS, Brockmann MD, Salamon J, Ittrich H, Hanganu-Opatz IL. Neonatal
823 hippocampal lesion alters the functional maturation of the prefrontal cortex and the
824 early cognitive development in pre-juvenile rats. *Neurobiol Learn Mem* **97**, 470-481
825 (2012).
- 826 67. Heyser CJ, Ferris JS. Object exploration in the developing rat: methodological
827 considerations. *Dev Psychobiol* **55**, 373-381 (2013).
- 828 68. Cichon NB, Denker M, Grun S, Hanganu-Opatz IL. Unsupervised classification of
829 neocortical activity patterns in neonatal and pre-juvenile rodents. *Front Neural*
830 *Circuits* **8**, 50 (2014).
- 831 69. Baccala LA, Sameshima K. Partial directed coherence: a new concept in neural
832 structure determination. *Biol Cybern* **84**, 463-474 (2001).
- 833 70. Baccala LA, Sameshima K, Takahashi DY. Generalized Partial Directed Coherence.
834 In: *2007 15th International Conference on Digital Signal Processing* (2007).

835 **Acknowledgements**

836 We thank Dr. Joseph Gogos for providing the DISC1 mice. We also thank A. Marquardt, C.
837 Tietze, A. Dahlmann, and P. Putthoff for excellent technical assistance. This work was
838 funded by grants from the European Research Council (ERC-2015-CoG 681577 to I.L.H.-O.)
839 and the German Research Foundation (SPP 1665, SFB 936 B5 to I.L.H.-O).

840

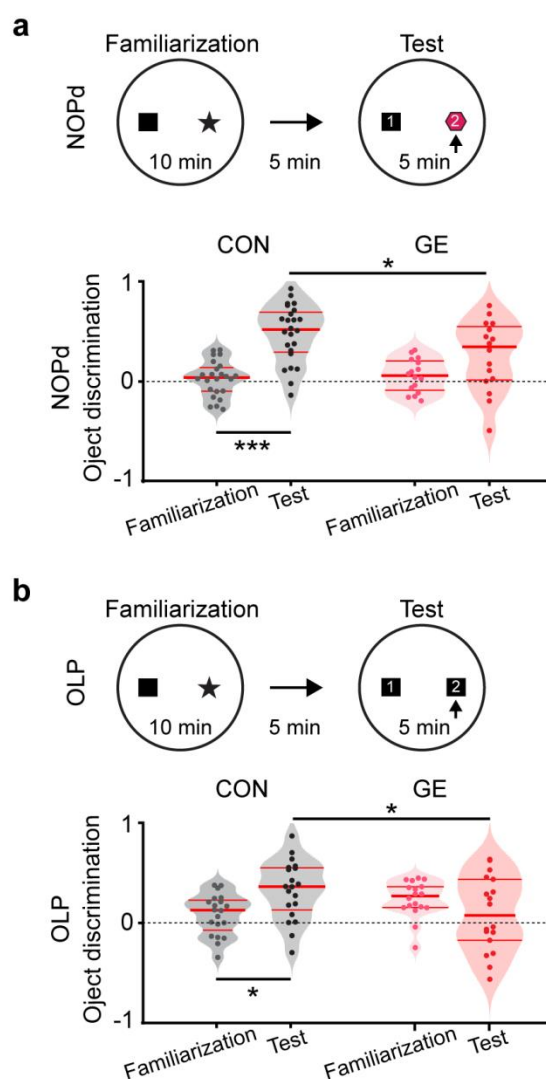
841 **Author contributions**

842 I.L.H.-O., X.X. designed the experiments, X.X., L.S., and R.K carried out the experiments,
843 X.X. analyzed the data, I.L.H.-O. and X.X. interpreted the data and wrote the paper. All
844 authors discussed and commented on the manuscript.

845

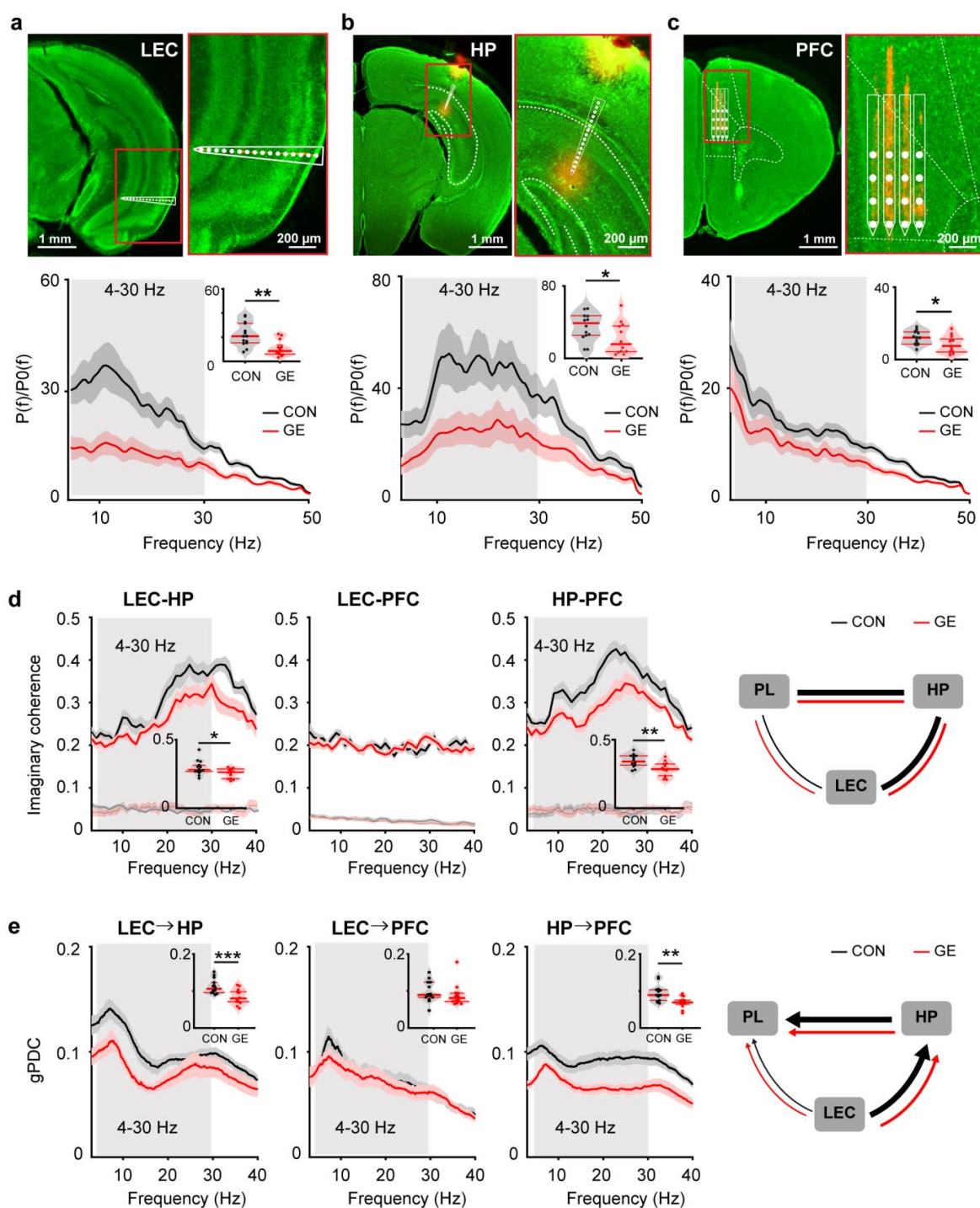
846 **Competing interests**

847 The authors declare no competing financial interests.



848

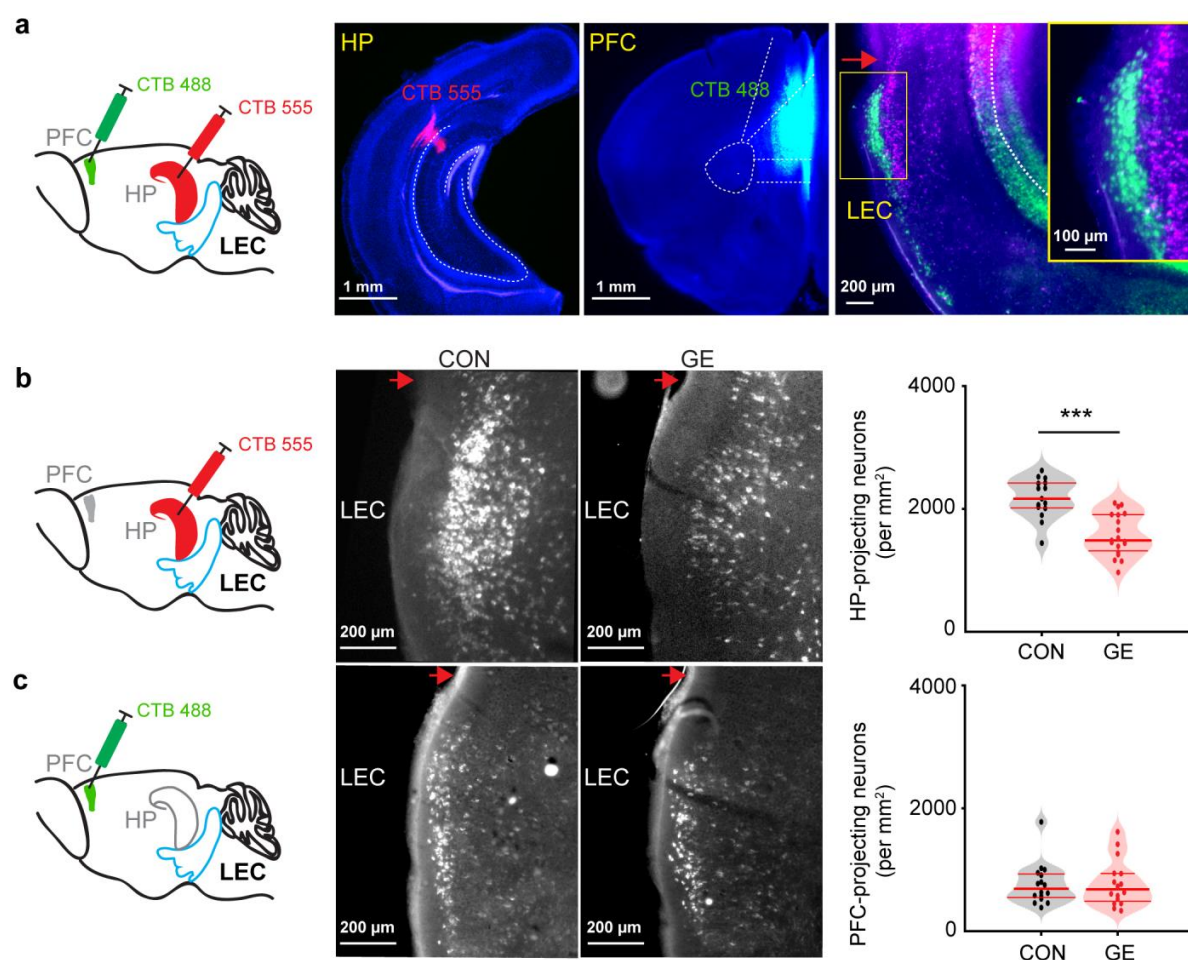
849 **Fig. 1 The performance of pre-juvenile GE mice in associative recognition memory**
 850 **tasks. (a)** Schematic of the protocol for NOPd task (top) and violin plots displaying the
 851 discrimination ratio in familiarization and test trials when averaged for CON and GE mice
 852 (bottom). **(b)** Schematic of the protocol for OLP task (top) and violin plots displaying the
 853 discrimination ratio in familiarization and test trials when averaged for CON and GE mice
 854 (bottom). In **(a)** and **(b)**, the black dotted line indicates chance level. Single data points are
 855 shown as dots and the red horizontal lines in violin plots correspond to the median and the
 856 25th and 75th percentiles. * $p < 0.05$, *** $p < 0.0001$.



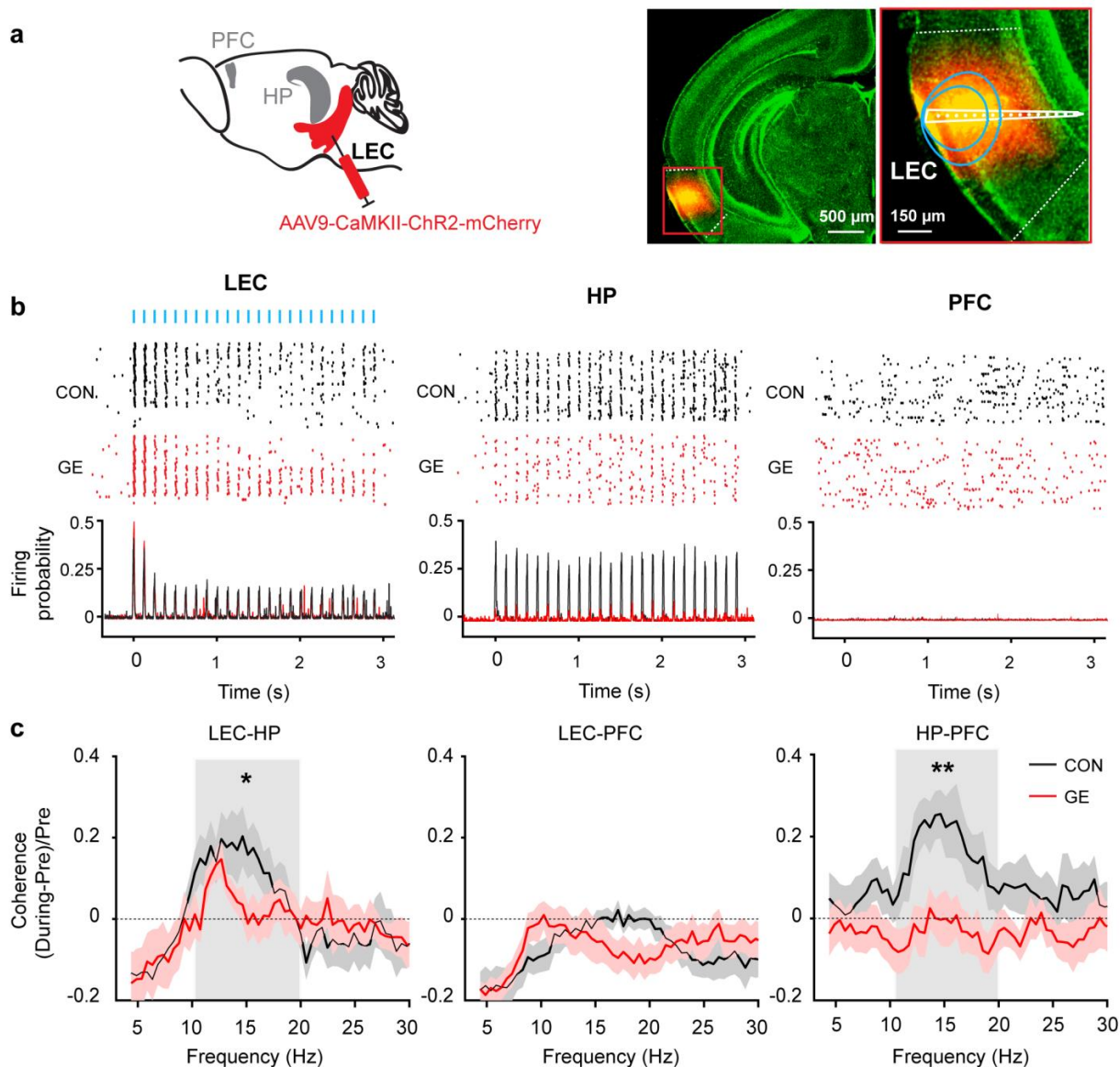
857
 858 **Fig. 2 Patterns of network activity in LEC, HP and PFC as well as functional**
 859 **communication within LEC-HP-PFC networks from neonatal CON and GE mice. (a)**
 860 Digital photomontage reconstructing the location of the Dil-labeled 1×16-site recording
 861 electrode (orange) in a 100 μm-thick coronal section containing the LEC from a P9 mouse.
 862 Right, the position of recording sites (white dots) over LEC layers when displayed at higher
 863 magnification. Bottom, averaged power spectra $P(f)$ of discontinuous oscillatory activity
 864 normalized to the baseline power $P_0(f)$ of time windows lacking oscillatory activity in CON

865 and GE mice. Inset, violin plots displaying the average power spectra from 1-50 Hz in CON
866 and GE mice. **(b)** Same as **(a)** for HP. **(c)** Same as **(a)** for PFC. **(d)** Line plots of mean
867 imaginary coherence for oscillatory activity simultaneously recorded in the LEC and HP, LEC
868 and PFC, as well as HP and PFC of CON (black) and GE (red) mice. The bottom lines in the
869 coherence plots correspond to the imaginary coherence calculated from shuffled data. Insets
870 for each coherence plot, violin plots displaying the imaginary coherence when averaged for
871 4-30 Hz. Right, schematic of synchrony within LEC-HP-PFC networks during neonatal
872 development as resolved by imaginary coherence. The line thickness indicates the strength
873 of the coupling between brain regions. **(e)** Same as **(d)** when the directional coupling within
874 LEC-HP-PFC networks was estimated by gPDC. Single data points are shown as dots and
875 the red horizontal bars in violin plots correspond to the median and the 25th and 75th
876 percentiles. * $p < 0.05$, ** $p < 0.01$, *** $p < 0.001$.

877



878
 879 **Fig.3 Long-range monosynaptic axonal projections connecting neonatal LEC,**
 880 **hippocampal CA1, and PFC. (a)** Schematic of the retrograde tracer CTB488 injection in
 881 PFC and CTB555 injection in HP. Digital photomontage showing the CTB555 injection in the
 882 HP (left) and CTB488 injection in the PFC (middle) of a P10 CON mouse. Right, digital
 883 photomontage displaying CTB555- (red) and CTB488- (green) labeled neurons in LEC of the
 884 same mouse. Inset, labeled neurons in LEC shown at higher-magnification. The red arrow
 885 indicates rhinal fissure. **(b)** Left, schematic of the retrograde tracer CTB555 injection in HP.
 886 Middle, photographs depicting CTB555-labeled neurons (white dot) in the LEC of a P10
 887 CON and GE mouse. Right, violin plot displaying the number of CTB555-labeled neurons in
 888 the LEC of CON and GE mice. **(c)** Same as **(b)** for CTB488 injection in PFC. Single data
 889 points (i.e. density of labeled neurons in LEC / slice) are shown as dots and red horizontal
 890 bars in violin plots correspond to the median and the 25th and 75th percentiles. *** $p < 0.001$.



891
892 **Fig. 4 Light-induced activation of LEC.** (a) Schematic of AAV9-CaMKII-ChR2-mCherry
893 injection in the LEC. Right, photographs depicting the injection position in the LEC of a P10
894 CON mouse and the position of injection site (red) shown at higher-magnification. Blue lines
895 correspond to the iso-contour lines for light power of 1 and 10 mW/mm², respectively. (b)
896 Representative raster plot and corresponding spike probability histogram for LEC, HP and
897 PFC in response to 120 sweeps of 8 Hz pulse stimulation (3 ms pulse length, 473 nm) in
898 LEC. (c) Line plots of coherence between LEC and HP, LEC and PFC, and HP and PFC
899 during ramp stimulation of LEC pyramidal neurons normalized to coherence values before
900 stimulation. Single data points are shown as dots. * $p < 0.05$, ** $p < 0.01$.

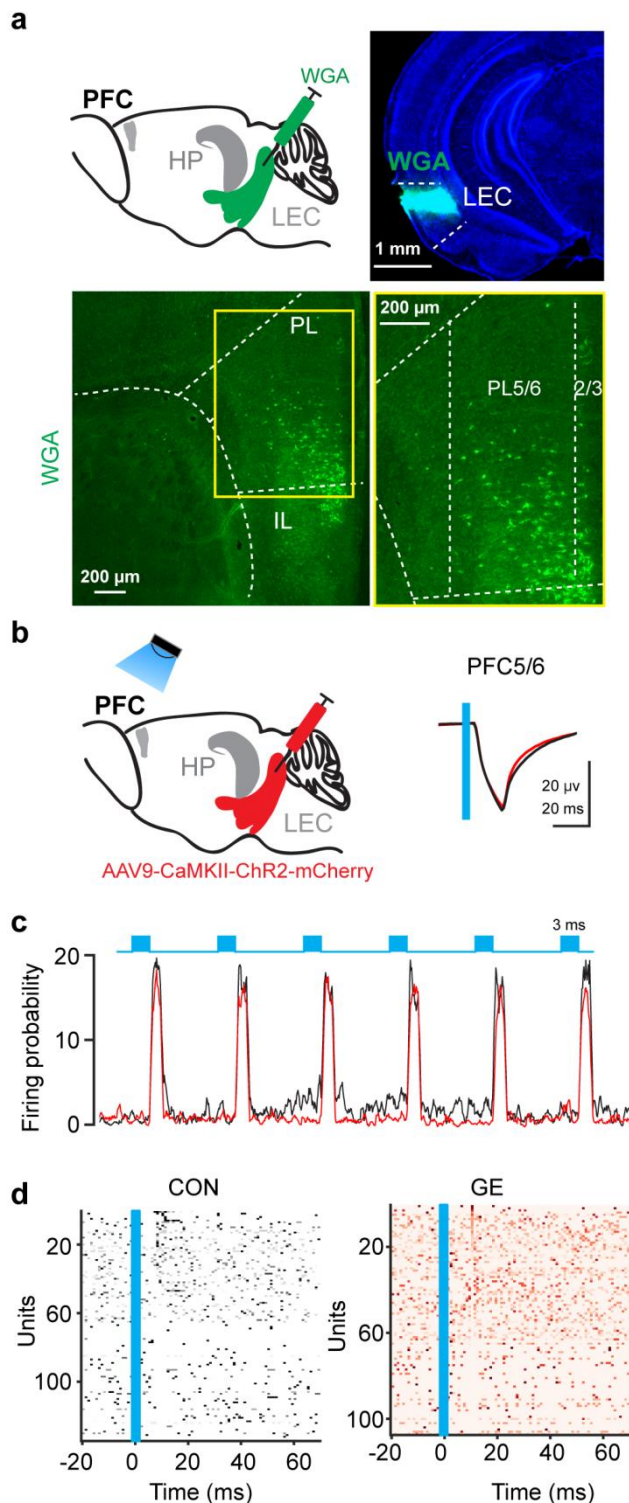


Fig. 5 Prelimbic neurons innervated by LEC and light-induced activation of LEC terminals in PFC. (a) Schematic of the anterograde trans-synaptic WGA injection in LEC. Photograph depicting the injection position in LEC of a P10 CON mouse. Bottom left, photographs depicting WGA-expressing neurons (green dots) in the PFC of a P10 CON mouse. Bottom right, WGA-labeled neurons in prelimbic layers displayed at a higher-magnification. PL, prelimbic subdivision of the PFC; IL, infralimbic subdivision of the PFC. (b) Schematic of the AAV9-CaMKII-ChR2-mCherry injection in the LEC and light stimulation of entorhinal axonal terminals in PFC. Right, averaged LFP traces recorded in the prelimbic layer 5/6 in response to light stimulation of LEC terminals in CON (black) and GE (red) mice. The blue line indicates the 3 ms-long pulse stimulation in PFC. (c) Spike probability histogram of prelimbic layer 5/6 neurons in response to 120 sweeps of 8 Hz pulse stimulation (3 ms pulse length, 473 nm, blue line) in CON (black) and GE mice (red). (d) Raster plot depicting the firing of single cells in response to the first pulse stimulation from each sweep in CON and GE groups. The blue line corresponds to the 3 ms-long pulse stimulation in PFC.

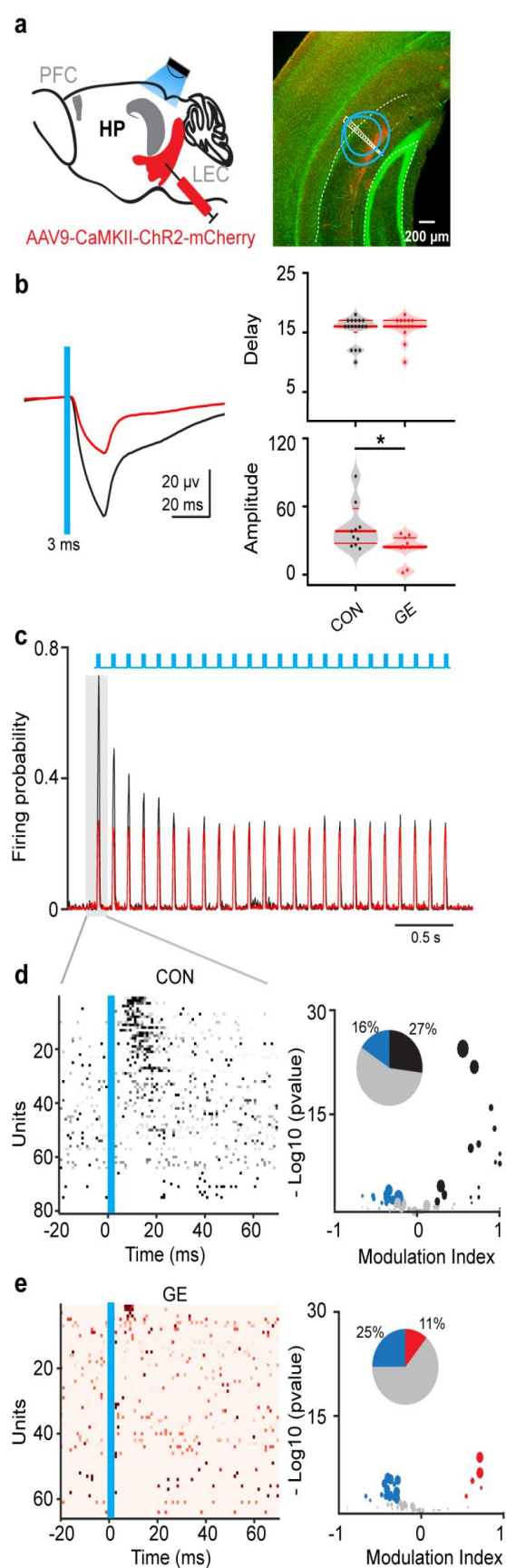
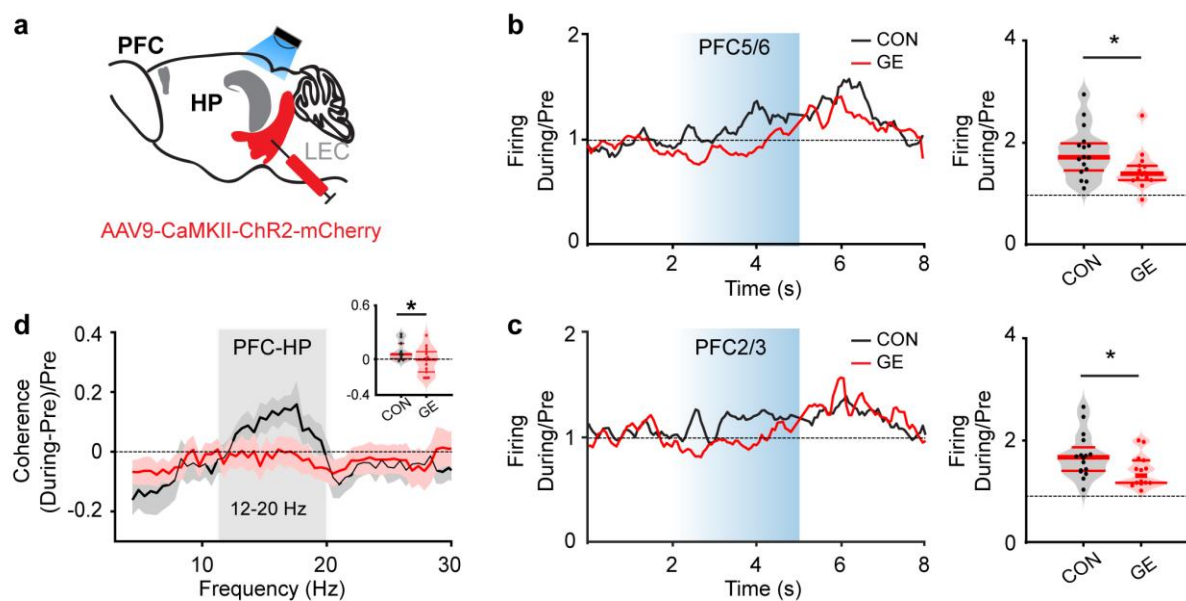


Fig. 6 Light-induced activation of LEC terminals in HP. (a) Schematic of the AAV9-CaMKII-ChR2-mCherry injection in LEC and light stimulation of entorhinal axonal terminals in HP. Right, photographs depicting the LEC axonal terminals labeled by mCherry (red) in the HP of a P9 CON mouse. Blue lines correspond to the iso-contour lines for light power of 1 and 10 mW/mm², respectively. (b) Averaged LFP traces recorded in the HP in response to light stimulation of LEC terminals in CON (black) and GE (red) mice. The blue line indicates the 3 ms-long pulse stimulation in HP. Right up, violin plots displaying the delay of the biggest response of the averaged LFP in HP. Right bottom, violin plots displaying the amplitude of the biggest response of the averaged LFP in HP. (c) Spike probability histogram for hippocampal neurons in response to 120 sweeps of 8 Hz pulse stimulation (3 ms pulse length, 473 nm, blue line) in CON (black) and GE (red) mice. (d) Left, raster plot depicting the firing of single hippocampal cells in response to the first pulse stimulation from each sweep in CON group. Right, the modulation index of spiking response of hippocampal single units to pulse stimulation. Modulation index > 0 indicates increased firing activity, whereas values < 0 correspond to decreased firing activity. Inset, pie plot depicting the percentage of hippocampal single units activated (black), inhibited (blue), non-responded (gray) to the stimulation. (e) Same as (d) for GE mice. Single data points are shown as dots and the red horizontal bars in violin plots correspond to the median and the 25th and 75th percentiles. *p<0.05.



970
 971 **Fig. 7 Firing activity in PFC during light-induced activation of LEC terminals in HP. (a)**
 972 Schematic of AAV9-CaMKII-ChR2-mCherry injection in LEC and light stimulation of
 973 entorhinal axonal terminals in HP. **(b)** Line plot of firing activity of prelimbic layer 5/6 neurons
 974 during 3 s-long ramp stimulation (light blue shadow) of LEC terminals in HP normalized to
 975 the activity before stimulation for CON and GE mice. The horizontal dotted line corresponds
 976 to no changes of firing activity during the stimulation. Right, violin plots displaying the firing
 977 activity of prelimbic layer5/6 neurons during 3 s-long ramp stimulation normalized to the
 978 activity before stimulation. **(c)** Same as **(b)** for prelimbic layer 2/3 neurons. **(d)** Line plots of
 979 HP-PFC coherence calculated during ramp stimulation of entorhinal terminals in HP and
 980 normalized to coherence values before stimulation. Inset, violin plot displaying the averaged
 981 12-20 Hz coherence between HP and PFC during stimulation when normalized to coherence
 982 values before stimulation. Single data points are shown as dots and the red horizontal bars
 983 in violin plots correspond to the median and the 25th and 75th percentiles. * $p < 0.05$, ** $p < 0.01$.

		HP-projecting neurons			PFC-projecting neurons		
		CON	GE	<i>p</i>	CON	GE	<i>p</i>
Passive properties	RMP (mV)	-68.76 ± 8.19	-69.24 ± 7.44	0.12	-69.19 ± 4.47	-68.39 ± 5.47	0.99
	Cm (pF)	111.85 ± 21.99	118.96 ± 14.10	0.46	120.32 ± 22.02	119.53 ± 14.05	0.96
	Rin (MΩ)	606.99 ± 181.96	632.35 ± 102.39	0.62	481.20 ± 96.20	551.86 ± 93.68	0.27
	Tm (ms)	67.24 ± 14.21	72.86 ± 16.08	0.17	58.95 ± 12.47	68.01 ± 12.95	0.29
	AP threshold (mV)	-41.16 ± 7.06	-42.20 ± 2.84	0.71	-42.94 ± 2.61	-44.05 ± 2.57	0.57
Active Properties	AP amplitude (mV)	79.33 ± 5.29	77.88 ± 2.71	0.49	80.80 ± 3.38	81.21 ± 2.94	0.85
	Half-width (ms)	2.82 ± 0.45	2.61 ± 0.26	0.16	2.07 ± 0.31	1.92 ± 0.45	0.61
	Rheobase (pA)	45.61 ± 20.87	54.20 ± 16.42	0.69	56.07 ± 16.41	50.53 ± 8.27	0.49
	Firing frequency (Hz)	14.39 ± 4.53	14.79 ± 1.94	0.82	13.81 ± 3.05	16.67 ± 3.16	0.18

984

985 **Table 1. Passive and active membrane properties of neurons in LEC of neonatal CON and GE mice.**

986

Figures

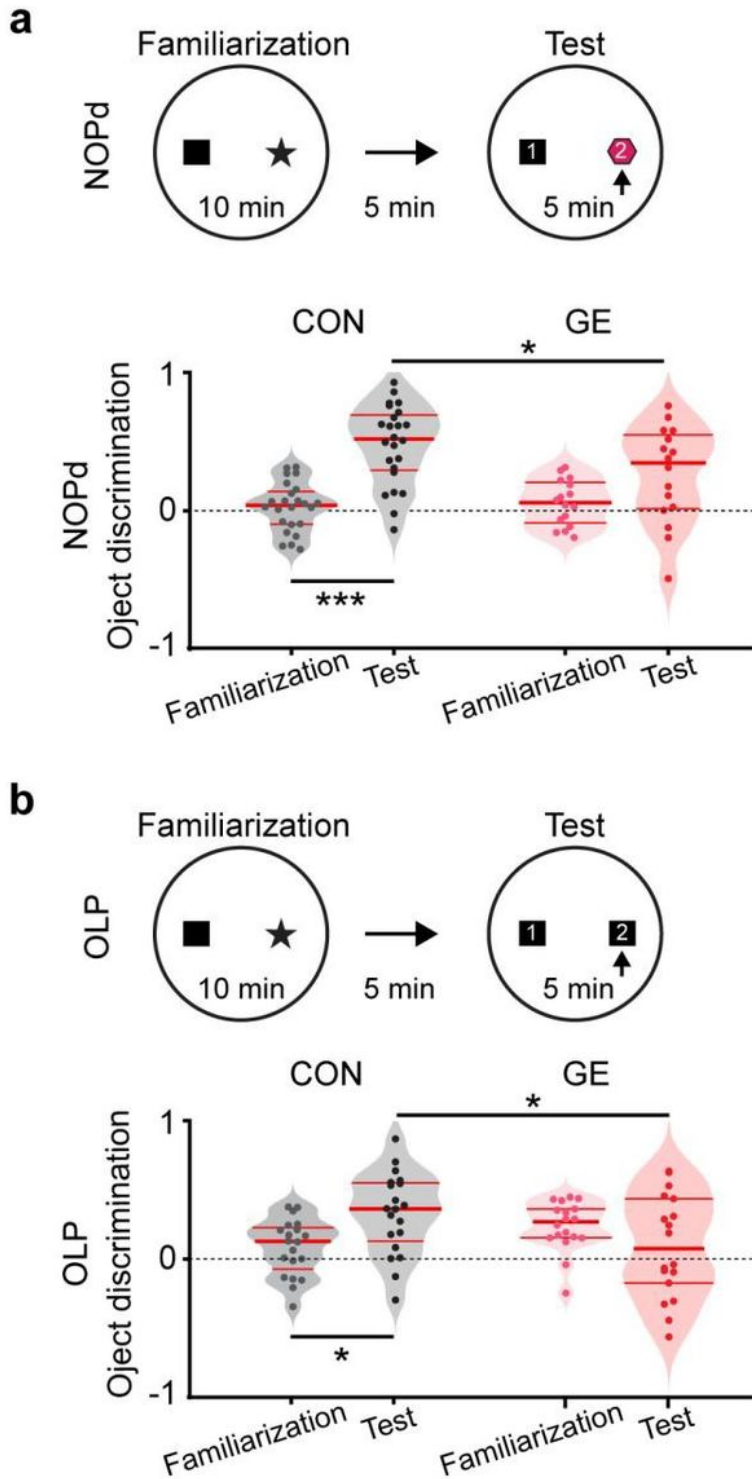


Figure 1

The performance of pre-juvenile GE mice in associative recognition memory tasks. (a) Schematic of the protocol for NOPd task (top) and violin plots displaying the discrimination ratio in familiarization and test trials when averaged for CON and GE mice (bottom). (b) Schematic of the protocol for OLP task (top) and

violin plots displaying the discrimination ratio in familiarization and test trials when averaged for CON and GE mice (bottom). In (a) and (b), the black dotted line indicates chance level. Single data points are shown as dots and the red horizontal lines in violin plots correspond to the median and the 25th and 75th percentiles. * $p < 0.05$, *** $p < 0.0001$.

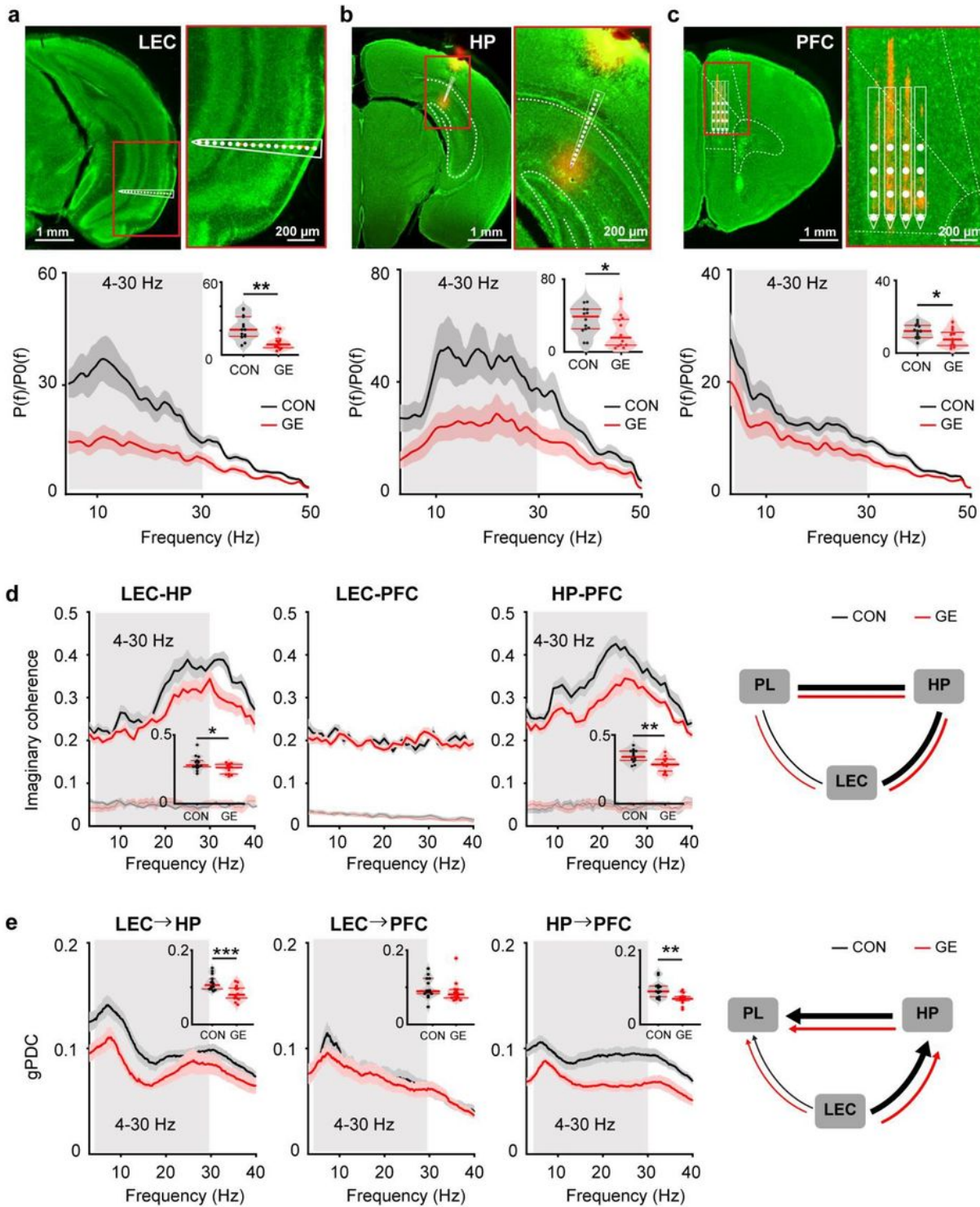


Figure 2

Patterns of network activity in LEC, HP and PFC as well as functional communication within LEC-HP-PFC networks from neonatal CON and GE mice. (a) Digital photomontage reconstructing the location of the Dil-labeled 1×16-site recording electrode (orange) in a 100 μm-thick coronal section containing the LEC from a P9 mouse. Right, the position of recording sites (white dots) over LEC layers when displayed at higher magnification. Bottom, averaged power spectra $P(f)$ of discontinuous oscillatory activity normalized to the baseline power $P_0(f)$ of time windows lacking oscillatory activity in CON and GE mice. Inset, violin plots displaying the average power spectra from 1-50 Hz in CON and GE mice. (b) Same as (a) for HP. (c) Same as (a) for PFC. (d) Line plots of mean imaginary coherence for oscillatory activity simultaneously recorded in the LEC and HP, LEC and PFC, as well as HP and PFC of CON (black) and GE (red) mice. The bottom lines in the coherence plots correspond to the imaginary coherence calculated from shuffled data. Insets for each coherence plot, violin plots displaying the imaginary coherence when averaged for 4-30 Hz. Right, schematic of synchrony within LEC-HP-PFC networks during neonatal development as resolved by imaginary coherence. The line thickness indicates the strength of the coupling between brain regions. (e) Same as (d) when the directional coupling within LEC-HP-PFC networks was estimated by gPDC. Single data points are shown as dots and the red horizontal bars in violin plots correspond to the median and the 25th and 75th percentiles. * $p < 0.05$, ** $p < 0.01$, *** $p < 0.001$.

are shown as dots and red horizontal bars in violin plots correspond to the median and the 25th and 75th percentiles. *** $p < 0.001$.

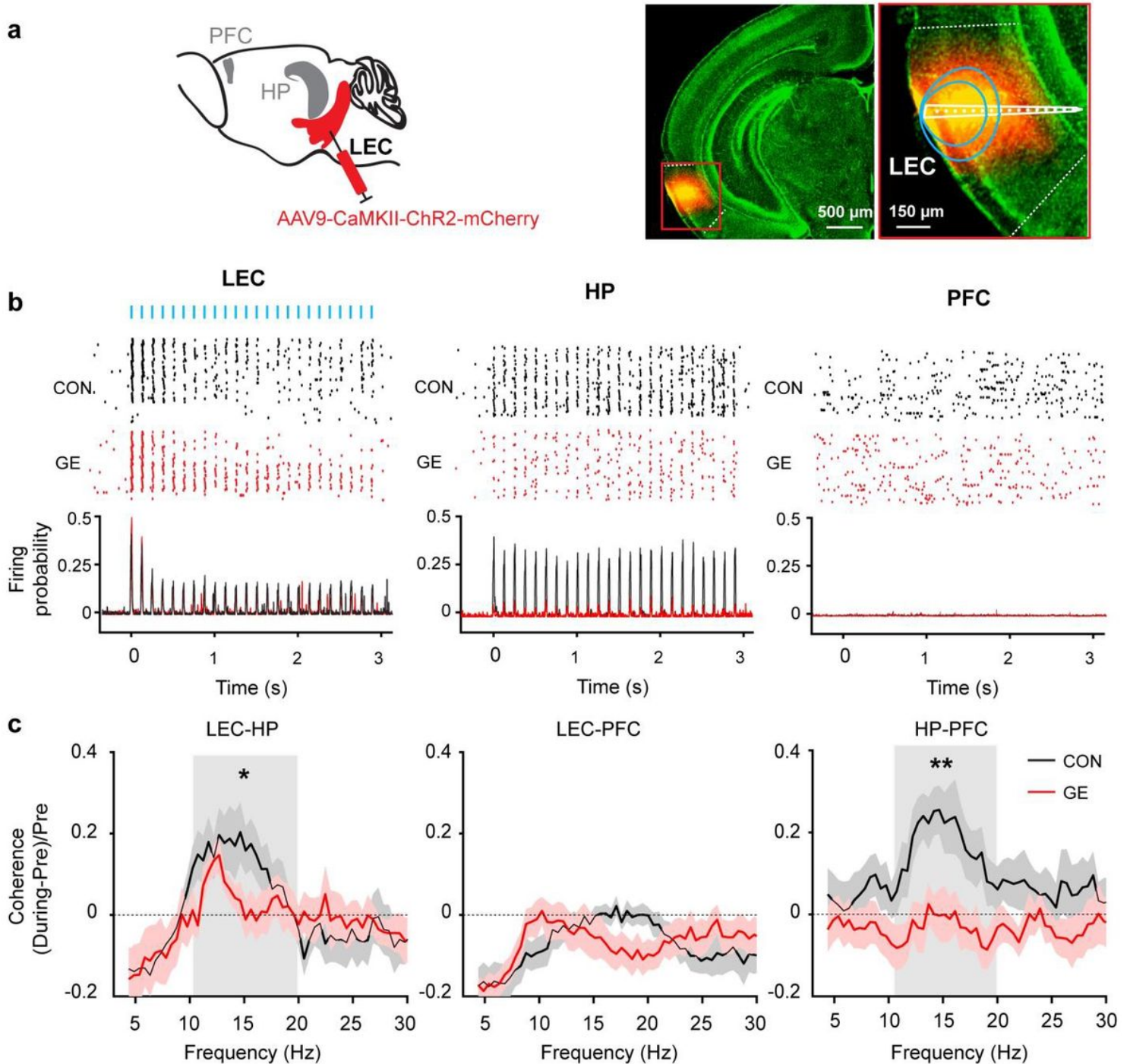


Figure 4

Light-induced activation of LEC. (a) Schematic of AAV9-CaMKII-ChR2-mCherry injection in the LEC. Right, photographs depicting the injection position in the LEC of a P10 CON mouse and the position of injection site (red) shown at higher-magnification. Blue lines correspond to the iso-contour lines for light power of 1 and 10 mW/mm^2 , respectively. (b) Representative raster plot and corresponding spike probability

histogram for LEC, HP and PFC in response to 120 sweeps of 8 Hz pulse stimulation (3 ms pulse length, 473 nm) in LEC. (c) Line plots of coherence between LEC and HP, LEC and PFC, and HP and PFC during ramp stimulation of LEC pyramidal neurons normalized to coherence values before stimulation. Single data points are shown as dots. * $p < 0.05$, ** $p < 0.01$.

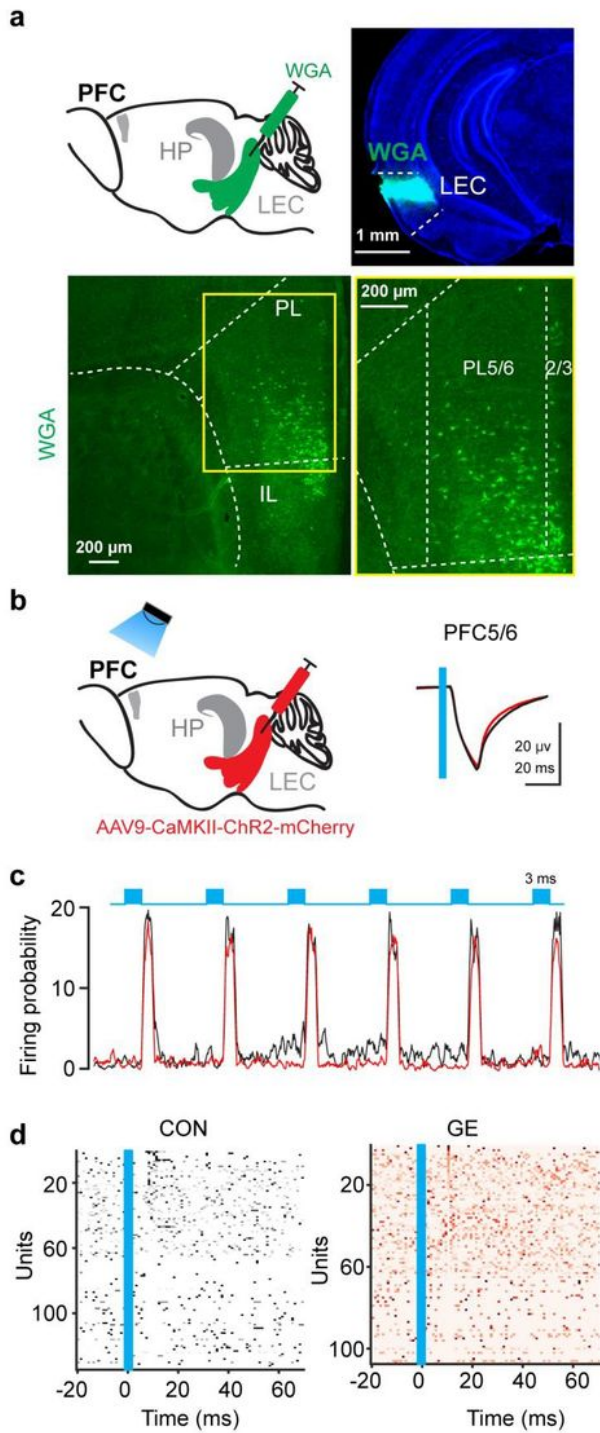


Figure 5

Prelimbic neurons innervated by LEC and light-induced activation of LEC terminals in PFC. (a) Schematic of the anterograde trans-synaptic WGA injection in LEC. Photograph depicting the injection position in LEC of a P10 CON mouse. Bottom left, photographs depicting WGA-expressing neurons (green dots) in the PFC of a P10 CON mouse. Bottom right, WGA-labeled neurons in prefrontal layers displayed at a higher-magnification. PL, prelimbic subdivision of the PFC; IL, infralimbic subdivision of the PFC. (b) Schematic of the AAV9-CaMKII-ChR2-mCherry injection in the LEC and light stimulation of entorhinal axonal terminals in PFC. Right, averaged LFP traces recorded in the prelimbic layer 5/6 in response to light stimulation of LEC terminals in CON (black) and GE (red) mice. The blue line indicates the 3 ms-long pulse stimulation in PFC. (c) Spike probability histogram of prelimbic layer 5/6 neurons in response to 120 sweeps of 8 Hz pulse stimulation (3 ms pulse length, 473 nm, blue line) in CON (black) and GE mice (red). (d) Raster plot depicting the firing of single cells in response to the first pulse stimulation from each sweep in CON and GE groups. The blue line corresponds to the 3 ms-long pulse stimulation in PFC.

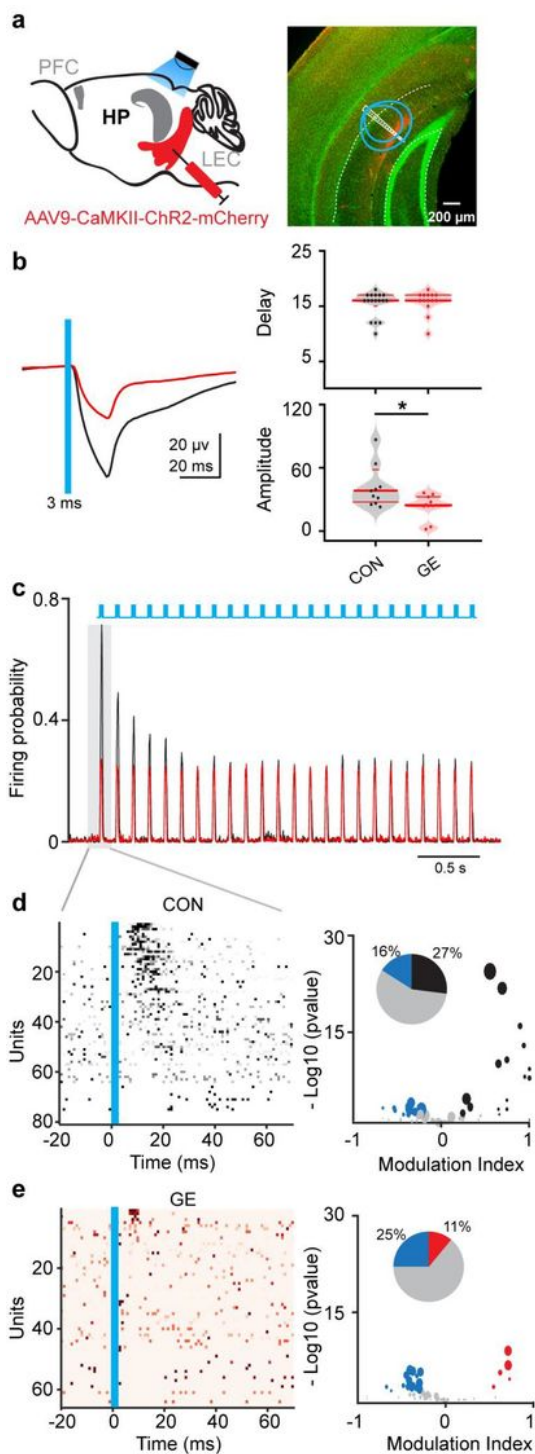


Figure 6

Light-induced activation of LEC terminals in HP. (a) Schematic of the AAV9-CaMKII-ChR2-mCherry injection in LEC and light stimulation of entorhinal axonal terminals in HP. Right, photographs depicting the LEC axonal terminals labeled by mCherry (red) in the HP of a P9 CON mouse. Blue lines correspond to the iso-contour lines for light power of 1 and 10 mW/mm², respectively. (b) Averaged LFP traces recorded in the HP in response to light stimulation of LEC terminals in CON (black) and GE (red) mice. The blue line

indicates the 3 ms- long pulse stimulation in HP. Right up, violin plots displaying the delay of the biggest response of the averaged LFP in HP. Right bottom, violin plots displaying the amplitude of the biggest response of the averaged LFP in HP. (c) Spike probability histogram for hippocampal neurons in response to 120 sweeps of 8 Hz pulse stimulation (3 ms pulse length, 473 nm, blue line) in CON (black) and GE (red) mice. (d) Left, raster plot depicting the firing of single hippocampal cells in response to the first pulse stimulation from each sweep in CON group. Right, the modulation index of spiking response of hippocampal single units to pulse stimulation. Modulation index > 0 indicates increased firing activity, whereas values < 0 correspond to decreased firing activity. Inset, pie plot depicting the percentage of hippocampal single units activated (black), inhibited (blue), non-responded (gray) to the stimulation. (e) Same as (d) for GE mice. Single data points are shown as dots and the red horizontal bars in violin plots correspond to the median and the 25th and 75th percentiles. * $p < 0.05$.

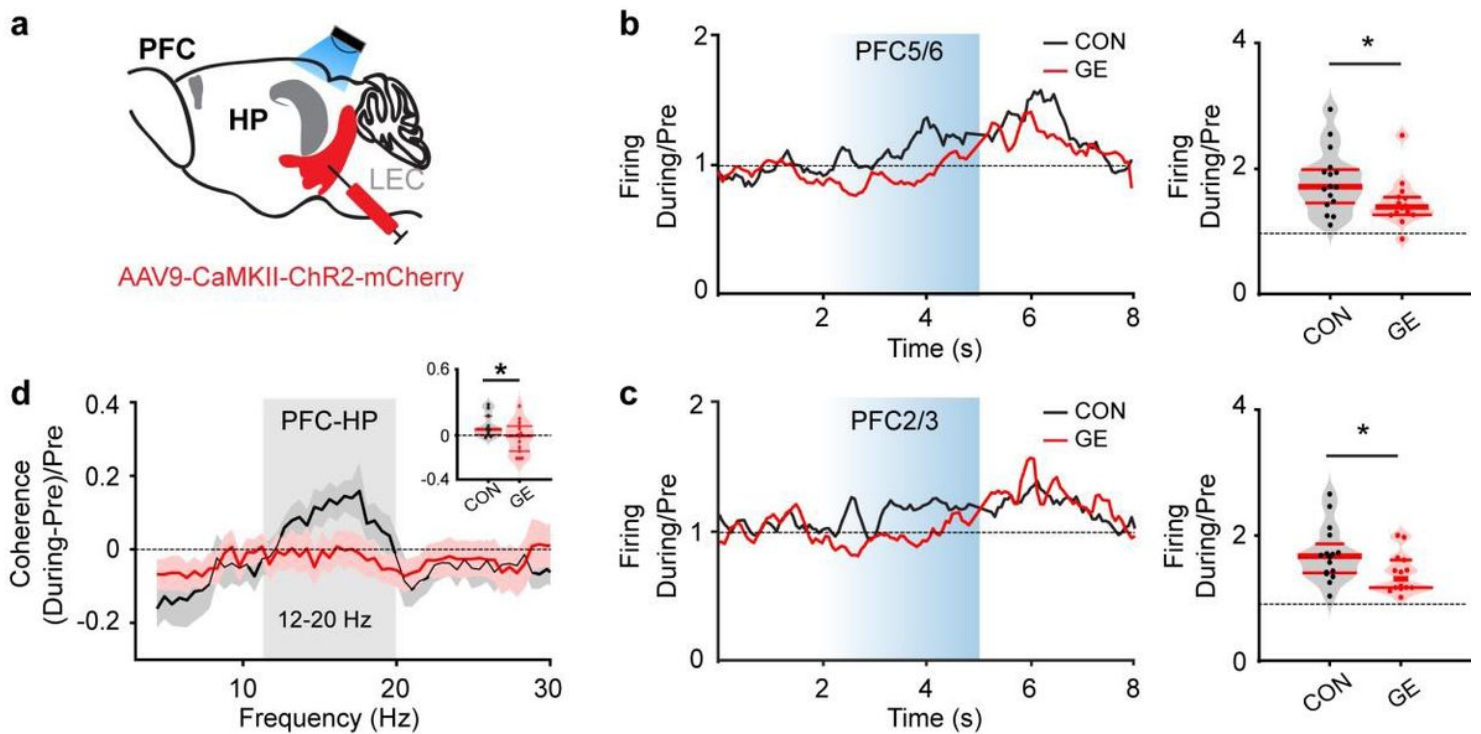


Figure 7

Firing activity in PFC during light-induced activation of LEC terminals in HP. (a) Schematic of AAV9-CaMKII-ChR2-mCherry injection in LEC and light stimulation of entorhinal axonal terminals in HP. (b) Line plot of firing activity of prelimbic layer 5/6 neurons during 3 s-long ramp stimulation (light blue shadow) of LEC terminals in HP normalized to the activity before stimulation for CON and GE mice. The horizontal dotted line corresponds to no changes of firing activity during the stimulation. Right, violin plots displaying the firing activity of prelimbic layer 5/6 neurons during 3 s-long ramp stimulation normalized to the activity before stimulation. (c) Same as (b) for prelimbic layer 2/3 neurons. (d) Line plots of HP-PFC coherence calculated during ramp stimulation of entorhinal terminals in HP and normalized to coherence values before stimulation. Inset, violin plot displaying the averaged 12-20 Hz coherence between HP and

PFC during stimulation when normalized to coherence values before stimulation. Single data points are shown as dots and the red horizontal bars in violin plots correspond to the median and the 25th and 75th percentiles. * $p < 0.05$, ** $p < 0.01$.

Supplementary Files

This is a list of supplementary files associated with this preprint. Click to download.

- [Supplementaryinformation.pdf](#)